

**FACULTY  
OF MATHEMATICS  
AND PHYSICS**  
Charles University

**BACHELOR THESIS**

Daniel Broško

**The Hydrofracturing of the Outer Shells  
of Icy Moons**

Mathematical Institute of Charles University

Supervisor of the bachelor thesis: RNDr. Ondřej Souček, Ph.D.

Study program: Physics

Study branch: General Physics

Prague 2021

I declare that I carried out this bachelor thesis independently, and only with the cited sources, literature and other professional sources. It has not been used to obtain another or the same degree.

I understand that my work relates to the rights and obligations under the Act No. 121/2000 Sb., the Copyright Act, as amended, in particular the fact that the Charles University has the right to conclude a license agreement on the use of this work as a school work pursuant to Section 60 subsection 1 of the Copyright Act.

In Prague date 22.07.2021

Author's signature

First of all, I would like to express my sincere gratitude to my supervisor, RNDr. Ondřej Souček, Ph.D., without whom this thesis would not see the light of the day. Thank you for your friendly approach, patience, continuous support, and the invaluable advice during consultations. I want to thank Charles University, especially the Faculty of Mathematics and Physics, for the opportunity to study such beautiful science as physics in the magnificent city of Prague and all the professors and faculty staff for their advice, exciting interpretation, and shared knowledge. My sincere thanks must also go to my family, who have always supported me and made my studies possible. I am also incredibly grateful for my friends, who have always stood by my side, never let me down, and motivate me to work harder. Last but not least, I would like to express my gratitude to everyone who helped me with or contributed to this thesis.

Title: The Hydrofracturing of the Outer Shells of Icy Moons

Author: Daniel Broško

Institute: Mathematical Institute of Charles University

Supervisor: RNDr. Ondřej Souček, Ph.D., Mathematical Institute of Charles University

Consultant: RNDr. Klára Kalousová, Ph.D., Charles University, Faculty of Mathematics and Physics, Department of Geophysics

Abstract: This thesis studies the continuum poro-damage mechanics (CPDM) and its application in the ice crack propagation model. The model is tested by the finite element method implementation - using the open-source library package FEniCS. The study examines the model's sensitivity and the crack depth on model parameters for a water-free crack. Furthermore, the thesis concentrates on the effect of applied additional longitudinal stress. Lastly, the model is tested on a water-filled crevasse. The water-free and water-filled cases follow the known theoretical predictions by the linear elastic fracture mechanics (LEFM), particularly considering deeper crevasses in the water-free case.

Keywords: hydrofracturing, icy moons, continuum poro-damage mechanics

# Contents

<b>Introduction</b>	<b>2</b>
<b>1 Model Formulation and Implementation</b>	<b>4</b>
1.1 Continuum Damage Mechanics Approach . . . . .	4
1.2 Model Formulation . . . . .	8
1.2.1 Geometry . . . . .	9
1.2.2 Governing Equations . . . . .	9
1.2.3 Initial and Boundary Conditions . . . . .	10
1.2.4 The Overview of Physical Parameters . . . . .	10
1.3 Numerical Implementation . . . . .	11
1.3.1 The Finite Element Method . . . . .	11
1.3.2 Weak Formulation . . . . .	12
1.3.3 FEniCS . . . . .	12
<b>2 Numerical Experiments</b>	<b>15</b>
2.1 Water-free Crevasse Propagation and Sensitivity to Model Parameters . . . . .	15
2.2 The Dependence of the Water-free Crevasse Depth on Model Parameters . . . . .	20
2.3 The Effect of Applied Longitudinal Stress . . . . .	27
2.3.1 The Damage and the Crevasse Depth Evolution . . . . .	27
2.3.2 The Evolution of Other Model Relevant Physical Quantities . . . . .	30
2.4 Water-free vs. Water-filled Crevasse . . . . .	41
<b>Conclusion</b>	<b>44</b>
<b>Bibliography</b>	<b>45</b>
<b>List of Figures</b>	<b>48</b>
<b>List of Tables</b>	<b>49</b>
<b>List of Abbreviations</b>	<b>50</b>
<b>A Attachments</b>	<b>51</b>
A.1 The LEFM Approach . . . . .	51

# Introduction

Hydrofracturing is a process of fracture propagation in a medium assisted by fluid pressure inside the fractures. On Earth, this process plays an essential role in the calving of the ice shelves and has been shown to allow for very rapid drainage of supraglacial lakes (e.g. Krawczynski et al., 2009), and in a much more exotic context, such drainage mechanism could be active in the outer water-ice shells of water worlds such as Jupiter’s moon Europa or Saturn’s Enceladus.

There are several important differences between the hydrofracturing processes on Earth and icy moons, however. On terrestrial glaciers, a fracture typically originates on the top of the glacier, where dynamic stresses may bring the ice to a tensional regime. Due to surface melting, crevasses may easily get filled with liquid water, which then further facilitates crack propagation downwards, possibly all the way to the glacier bed. The physical setting on icy moons is very different - the very low surface temperature (approx. 100 K for Europa (Ojakangas and Stevenson, 1989) or approx. 59 K for Enceladus, (Beuthe, 2018)), do not allow for any meltwater on the surface. Melt, if produced at all, would most likely appear deeper in bulk or at strike-slip fault due to mechanical dissipation (Kalousová et al., 2016). At these depths, typically a few kilometers below the surface, hydrofracturing becomes less likely due to the overburden pressure limiting crack initiation. Also, even if cracks would develop, the predicted meltwater production rates are lower by few orders of magnitude compared to the terrestrial supply during the melting season (Hock, 2005). Consequently, the resulting meltwater supply would be most likely insufficient to feed the crevasses by an appropriate amount of meltwater required for hydrofracturing across the whole ice layer, particularly when competing with possibly rapid re-freezing in the cold environment.

However, it has been hypothesized that fractures could propagate upwards from the internal oceans under suitable dynamic conditions as the ocean body would provide an effectively unlimited supply of meltwater. Crawford and Stevenson (1988) applied linear elastic fracture mechanics to investigate the possibility of upward propagation of water-filled cracks and also downward water-free crack propagation. While they exclude the possibility of water-free cracks extending across the whole ice shell, they argue that water-filled cracks propagating upwards might reach Europa’s surface provided they contain enough exsolved gas. Recently, Lee et al. (2005) and Rudolph and Manga (2009) revisited the subject of ice shell cracking under applied tensional stresses (e.g., due to tides, non-synchronous rotation, or ice shell thickening). While the former study found that surface cracks may penetrate through the entire outer brittle layer, the latter’s results indicate that the entire shell would be completely cracked only when sufficiently thin. Both of these studies study water-free cracks originating at the surface.

The original goal of this thesis was to investigate the possibility of crack initiation from below a subsurface liquid water ocean and quantify the dynamic conditions required to propagate the crack across the whole layer. We devise a numerical model of the process of fracture propagation based on the finite element numerical code developed by Duddu et al. (2020). If formulated in the frame-

work of continuum damage mechanics (CDM), the model couples the mechanical equations for ice with the evolution of an internal parameter, the damage, that characterizes the concentration of microcracks in the medium and represents a continuum counterpart to the notion of a crack within the material.

As it turned out during the work on this project, the original goal was too ambitious regarding the planetary applications. As a result, we shall remain in the terrestrial setting, studying downward crack propagation of a floating ice slab (ice shelf) in a suitably simplified setting, and we will focus on the study of effects of principal model parameters, the presence of water, and dynamical regime within the ice slab on the crack propagation process. We compare the results with the results predicted by the analytical estimates based on linear elastic fracture mechanics (LEFM), intending to quantitatively test the CDM approach and prepare the ground for future planetary applications.

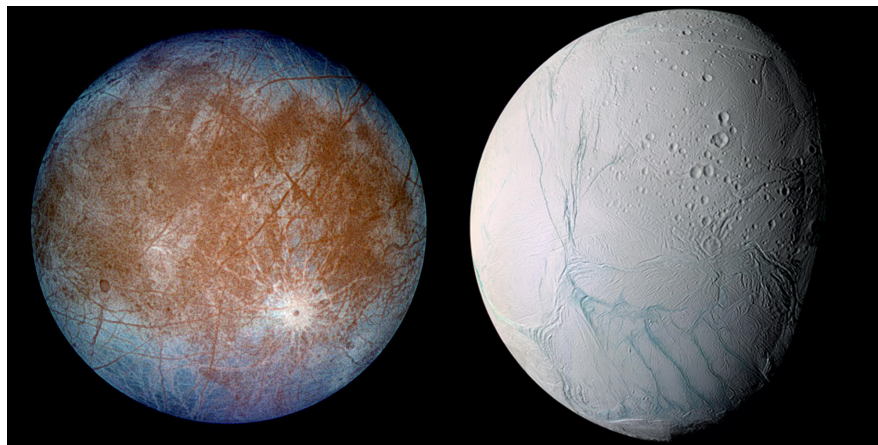


Figure 1: Europa and Enceladus. (Credit: NASA.)

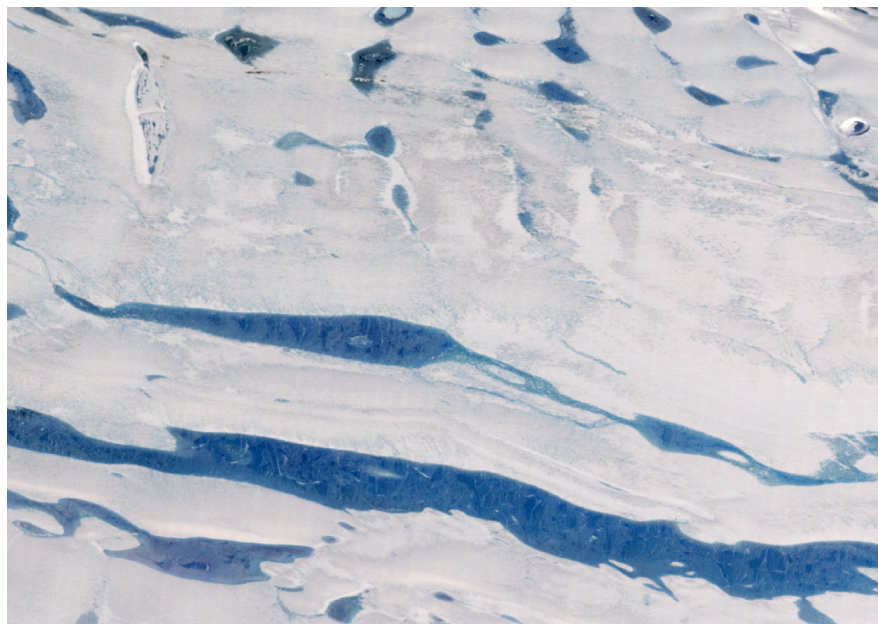


Figure 2: Hydrofracturing. (Credit: NASA.)

# 1. Model Formulation and Implementation

To understand the process of hydrofracturing in glaciers or planetary ice layers, we need a physically consistent model that can enable us to examine the conditions upon which the crevasse propagation or ice calving are possible. Traditionally, the problem of crack propagation in glaciers has been adopted in the framework of linear elastic fracture mechanics (LEFM), see, for instance - Smith (1976), Weertman (1973), van der Veen (1998a), van der Veen (1998b). Such an approach allows one to characterize crack propagation of a single crevasse in a typically semi-infinite elastic medium by analytical or semi-analytical estimates of stress conditions at the crevasse tip and by formulating crack propagation criteria.

Here, the goal is to investigate the problem of crack propagation by an alternative formulation - the continuum poro-damage mechanics (CPDM), formulated in Duddu et al. (2020), which characterizes the crack propagation in terms of an evolving scalar field  $D$  (damage), representing the density of microcracks in the material. A significant advantage of such an approach is that it allows for a unified continuum-mechanics formulation for the undamaged ice and the damaged one (representing the crack). This approach allows us to implement such a model by using the finite element method (FEM) and employ standard FEM tools.

In the following section, we will first introduce in detail the continuum poro-damage mechanics (CPDM) model by Duddu et al. (2020) and summarize the governing equations coupling the mechanical problem with the evolution of a damage  $D$ . We will discuss a specific variant of the model, which allows us to include the hydrofracturing, i.e., the effect of liquid water filling the microcracks on the stress field (thus on crack propagation, too).

## 1.1 Continuum Damage Mechanics Approach

Our model is based on the non-local continuum poro-damage mechanics (CPDM) model formulated in the study by Duddu et al. (2020) published in Journal of Glaciology. The CPDM model is broadly speaking an extension of the continuum damage mechanics (CDM) introduced in a series of papers by Jiménez et al. (2017) and Mobasher et al. (2016). In general, the CPDM model reduces unwanted mesh-size sensitivity and artificial diffusion of damage in crevasse propagation simulations that can occur if one uses the CDM model. The CPDM also provides feedback between viscous or elastic processes and damage processes at the crevasse tip.

In particular, in our model, the damage  $D$  variable is introduced as an isotropic scalar quantity that can acquire values between  $D = 0$  (represents an undamaged state) and  $D = 1$  (represents a fully damaged state). Therefore, by using the damage  $D$  variable, we can describe the level of material degradation at each material point in the continuum. Intuitively, continuum points with  $0 < D < 1$  describe areas, which can be interpreted as zones where the material is partially damaged (e.g., severe microcracks or microvoids), yet before failure. Areas with the damage variable  $D = 1$  represent an open crack after failure. Such a crack is

physically interpreted as an air-filled (or water-filled) crack.

Based on the principle of effective stress (Kachanov, 1958), (Rabotnov, 1963), and hypothesis of strain equivalence, the effective Cauchy stress tensor  $\bar{\boldsymbol{\sigma}}$  is defined as

$$\bar{\boldsymbol{\sigma}} = \frac{\boldsymbol{\sigma}}{(1 - D)}, \quad (1.1)$$

where  $\boldsymbol{\sigma}$  is Cauchy stress tensor. According to Duddu et al. (2020), in a finite thickness zone saturated with water within an otherwise undamaged ice slab, we interpret the isotropic damage  $D$  variable as the ratio of the area of microcracks and microvoids to the total area on a planar surface through representative volume element (RVE). Note that for  $D = 0$ , the effective Cauchy stress tensor coincides with the "classical" Cauchy stress tensor. On the other hand, assuming the partially damaged RVE - the effective Cauchy stress increase proportionally, which can be interpreted as the stress concentrating in the reduced area. From this point of view, the damage  $D$  variable is related to porosity  $\phi$ , which is defined as the ratio of the volume of microvoids to the total volume within RVE (analogically in 2D).

A damaged ice zone is usually partially filled with water; therefore Duddu et al. (2020) extend the CDM model by adding a hydrostatic pressure exerted by water in the crevasse. Microcracks and microvoids located in the damaged zone of the physical RVE are exposed to hydraulic pressure  $p_w$ , while the remaining undamaged ice sustains effective Cauchy stress. Consequently, we define the macroscopic Cauchy stress  $\boldsymbol{\sigma}$  in saturated damaged ice as given by Mobasher et al. (2016)

$$\boldsymbol{\sigma} = (1 - D)\bar{\boldsymbol{\sigma}} - D p_w \mathbf{I}, \quad (1.2)$$

where  $\mathbf{I}$  denotes the identity tensor. Depending on a particular application, ice is usually described by two different rheological models. On a short time scale (hours and less), ice is best characterized as a linear elastic (or viscoelastic) solid. On the other hand, glacier or ice-sheet over a long time period (days to years) flows as a non-linearly viscous (non-Newtonian) fluid. We decided to perform numerical simulations with "only" linear elastic rheology, despite investigating longer time periods. The reason is the difficulty and complexity of non-linear viscosity, but also the intention to make a quantitative comparison with the results predicted by the standard linear elastic fracture mechanics (LEFM) model. Assuming the ice to be incompressible, we can decompose the effective stress into deviatoric and volumetric parts as

$$\bar{\boldsymbol{\sigma}} = \bar{\boldsymbol{\tau}} - \bar{p} \mathbf{I}, \quad (1.3)$$

where  $\bar{p} = -\frac{1}{3} Tr[\bar{\boldsymbol{\sigma}}]$  is the effective pressure and  $\bar{\boldsymbol{\tau}}$  is the effective deviatoric Cauchy stress, determined by a constitutive model of a linear elastic solid (see equation 1.6 below).

The mechanical part of the problem is described by standard set of balance equations of continuum mechanics - the balance of mass, the balance of linear and angular momentum. The considered problem is formally formulated on a fixed domain. Thus, the Lagrangian (Martinec, 2019) description is appropriate. However, if assuming small deformations within linearized theory, one may neglect the differences between the Lagrangian and the Eulerian description and employ the latter, for simplicity. Assuming the incompressibility and neglecting the effect

of inertia, the balance of mass and linear momentum, respectively, yields

$$\nabla \cdot \mathbf{u} = 0, \quad (1.4)$$

$$\nabla \cdot \boldsymbol{\sigma} + \mathbf{b} = \mathbf{0}, \quad (1.5)$$

where  $\mathbf{u}$  is the displacement vector, the Cauchy stress tensor  $\boldsymbol{\sigma}$  is symmetric as a consequence of balance of angular momentum, and  $\mathbf{b}$  represents a body force.

If we consider the ice to be an isotropic and incompressible elastic solid, the deviatoric stress  $\bar{\boldsymbol{\tau}}$  can be defined as

$$\bar{\boldsymbol{\tau}} = \frac{E}{(1 + \nu)} \boldsymbol{\epsilon}. \quad (1.6)$$

where  $E$  represents the Young's modulus and  $\nu$  is the Poisson's ratio, and  $\boldsymbol{\epsilon}$  is the small strain tensor. Poisson's ratio for perfectly incompressible isotropic material deformed elastically at small strains is  $\nu = 0.5$ . The small strain tensor  $\boldsymbol{\epsilon}$  is defined as a symmetric gradient of the displacement field  $\mathbf{u}$

$$\boldsymbol{\epsilon} = \frac{1}{2} (\nabla \mathbf{u} + \nabla^T \mathbf{u}). \quad (1.7)$$

By combining equations 1.3 and 1.6 and substituting them into equation 1.2, we obtain the following rheological expression for the Cauchy stress tensor of a damaged ice filled with pressurized water

$$\boldsymbol{\sigma} = (1 - D) \left( \frac{E}{(1 + \nu)} \boldsymbol{\epsilon} - \bar{p} \mathbf{I} \right) - D p_w \mathbf{I}. \quad (1.8)$$

Note that the case  $D = 0$  describes undamaged ice, whereas  $D = 1$  yields the stress condition within the fully damaged ice - water- or air-filled crevasse. For the damage ( $D$ ) in the range between the mentioned values, the stress is determined as a combination of the solid ice stress and fluid water (air) stress according to their respective ratios.

To model time-dependent propagation of crevasse, we use the gradient non-local continuum damage mechanics formulation, first presented in Jiménez et al. (2017). The failure of ice is usually described by the progressive accumulation of micro-cracks and micro-voids. However, in our case - using the continuum damage mechanics, the law of crevasse propagation is formulated phenomenologically and does not explicitly identify void or crack growth or coalescence and other micro-mechanical mechanisms. The damage evolution law we take into account does not allow anisotropy dependent on micro-crack orientation induced by a damage, because the damage  $D$  variable is a scalar. Also in the considered model, we allow the damage  $D$  to increase only if the pressure is negative, which is equivalent to the material in a tensile stress state. According to Duddu et al. (2020), we define the material local damage time-derivative, which acts as a source term in the damage evolution equation (see eq. 1.14 below), as

$$\dot{D}^{\text{loc}} = \begin{cases} B \frac{\langle \bar{\chi} \rangle^r}{(1 - D)^{k_\sigma}} & \text{if } \bar{p} < 0, \\ 0 & \text{if } \bar{p} \geq 0. \end{cases} \quad (1.9)$$

Note that expression 1.9 cannot be negative (see below), therefore the model prohibits healing process of the material as the damage can only increase. Parameter  $B$  is a damage rate coefficient,  $r$  is a damage rate exponent and  $k_\sigma$ , which is experimentally calibrated, represents the local damage rate enhancement due to a prior damage. We use parameter  $B = 5.23 \times 10^{-7} \text{ MPa}^{-r} \cdot \text{s}^{-1}$ , assumed by Duddu and Waisman (2012). Parameter  $k_\sigma$  depends on the stress state, and is defined as

$$k_\sigma = k_1 + k_2 Tr[\boldsymbol{\sigma}], \quad (1.10)$$

where  $k_1$  and  $k_2$  are constants. In equation 1.9,  $\langle \bar{\chi} \rangle$  represents the positive part of the effective Hayhurst stress invariant (Hayhurst, 1972), (Murakami et al., 1988), defined as

$$\bar{\chi} = \alpha \bar{\sigma}^{(I)} + \beta \bar{\sigma}^v + (1 - \alpha - \beta) Tr[\bar{\boldsymbol{\sigma}}]. \quad (1.11)$$

Parameters  $\alpha$  and  $\beta$  determine brittle vs ductile regime of the crevasse propagation. In the definition of the effective Hayhurst stress invariant,  $\bar{\sigma}^{(I)}$  is the effective maximum principal stress, and  $\bar{\sigma}^v$  is the effective von Mises stress, defined as

$$\bar{\sigma}^{(I)} = \frac{\bar{\sigma}_{xx} + \bar{\sigma}_{yy}}{2} + \sqrt{\left(\frac{\bar{\sigma}_{xx} - \bar{\sigma}_{yy}}{2}\right)^2 + \bar{\tau}_{xy}^2}, \quad (1.12)$$

$$\bar{\sigma}^v = \sqrt{\frac{3}{2} \bar{\boldsymbol{\tau}} : \bar{\boldsymbol{\tau}}}, \quad (1.13)$$

where ":" represents the inner product.

Conditions set on the local damage rate in equation 1.9 allow the damage growth only in locations where the material is in a tensional regime. At the initial stages of crevasse propagation problem, the term  $(1 - D)^{k_\sigma}$  has usually no significant effect as  $D \ll 1$ . As a consequence, the damage rate is mainly determined by the Hayhurst stress  $\chi$ . The Hayhurst stress expresses the propagation and nucleation of the crevasse at sub-critical conditions ( $D < 1$ ) (Weiss, 2004).

Parameters that affect the value of the effective Hayhurst stress invariant, as can be seen in equation 1.11, are constrained by the condition  $\alpha + \beta \leq 1$ . For  $\alpha \rightarrow 1$ , the effective Hayhurst stress coincides with the maximum principal stress, which describes brittle failure behaviour. On the other side,  $\beta$  leads the Hayhurst stress invariant toward the von Mises stress, which describes ductile failure behaviour. Whereas no well calibrated values of these parameters are available, there are some estimates based on laboratory experiments, such as  $\alpha = 0.21$  and  $\beta = 0.63$  in (Pralong and Funk, 2005), which we used for this thesis. Parameters  $k_1, k_2$ , which evaluates  $k_\sigma$  parameter in equation 1.9 are also assumed from (Pralong and Funk, 2005),  $k_1 = -2.63$  and  $k_2 = 7.24 \text{ MPa}^{-1}$ .

A non-local implicit gradient formulation for the damage evolution is established (Jiménez et al., 2017) to maintain thermodynamic consistency and alleviate mesh-size sensitivity. The (material) time derivative of the damage is governed by the following elliptic equation

$$\dot{D} - \frac{1}{2} l_c^2 \Delta \dot{D} = \dot{D}_{\text{loc}}, \quad (1.14)$$

where a non-local length scale  $l_c$ , if appropriately chosen, protects the local damage model from the undesirably large dependency of the damage zone on the finite

element mesh size and other pathological mesh-size dependence. The principle behind this approach is based on the idea of smearing the damage within the damage zone in a regularized way, while  $l_c$  has to be sufficiently bigger than the finite element mesh size (Duddu and Waisman, 2013), which ensures thermodynamic consistency. Despite all, the length scale parameter  $l_c$  impacts the length of the fracture process zone ahead of the crack tip. As can be seen above, the suitable value of  $l_c$  is important. Following Duddu et al. (2020), we will adopt the estimate based on the article by A. Hillerborg et al. (1976)

$$l_c \approx \frac{K_{Ic}^2 (1 - \nu^2)}{\sigma_c^2}, \quad (1.15)$$

where  $K_{Ic}$  is the critical stress intensity factor and  $\sigma_c$  is the cohesive strength. The critical stress intensity factor is the parameter that well describes the fracture toughness of glacier ice, a typical range for  $K_{Ic}$  is  $0.1 - 0.4$  MPa m<sup>1/2</sup> (Paterson, 1994), (van der Veen, 1998b).

The cohesive strength  $\sigma_c$  has usually much lower values in comparison with the tensile yield strength of the ice, with various estimates - van der Veen (1998b) suggests it as the value of stress that necessary to form a crevasse, which puts  $\sigma_c$  in the range  $30 - 80$  kPa. Pralong and Funk (2005), and Krug et al. (2014) rather connect  $\sigma_c$  to a stress threshold necessary for damage initiation, which is in the range of  $10 - 200$  kPa. Given the above, we assume  $\sigma_c = 0.1$  MPa. This provides us with  $l_c \approx 0.75$  to  $12$  m (Weiss, 2003).

The continuum damage mechanics (CDM) allows us to transfer from a classical description of crack propagation in the framework of linear elastic fracture mechanics (LEFM) based on estimates of the stress at the crack tip and propagation criteria to a description by single scalar field  $D$  (damage) characterizing the density of microcracks. The evolution of this scalar field  $D$  is given by the effective Cauchy stress tensor  $\bar{\sigma}$ . Some of the advantages of such a model are validity for any arbitrary geometry (or boundary condition) of a glacier. In addition, no initial crack or damage is required to start to form and spread crevasses. Nevertheless, there are several important limitations of the CDM model. Difficulties come with parameters necessary for computation by the CDM approach - several empirical parameters cannot be precisely determined from yet existing measurements and observations, which directly affects the model's predictive capability. Furthermore, when the so-called full Stokes numerical formulation is considered to describe an ice flow, the CDM model is computationally expensive for investigating a crevasse propagation in a real glacier. However, using some effective adjustments (like higher-order Stokes approximations instead of full Stokes formulations) can reduce uncertainty. Therefore, the CDM model is a useful tool for a better understanding of the crevasse propagation problem when various physical conditions are taken into account.

## 1.2 Model Formulation

This section details the studied problem by defining the model's geometry, specifying the initial and boundary conditions, and providing the values of used material and model parameters.

## 1.2.1 Geometry

As a test case, we consider a two-dimensional freely floating ice slab with an initial surface crack propagating downwards. The considered modelling domain is a rectangular subdomain of the slab. The modelling subdomain is of dimensions  $500 \text{ m} \times 125 \text{ m}$  (length  $\times$  height). We assume the length-to-height aspect ratio of the whole ice slab to be very large (in accordance with the standard geometry of terrestrial ice shelves). The density of ice  $\rho_i$ , the density of water  $\rho_w$  and other related parameters are listed in table 1.1. The illustration of the model geometry is shown in figure 1.1.

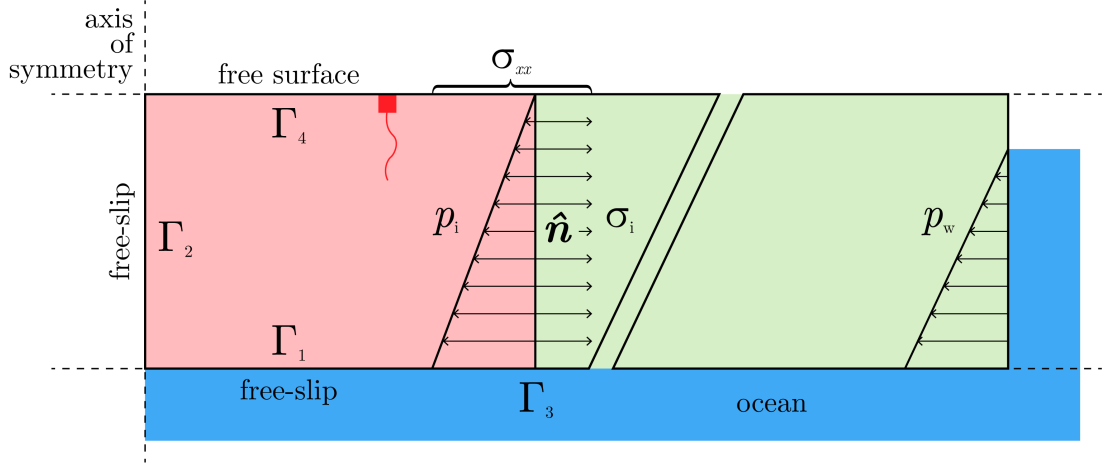


Figure 1.1: The illustration of a studied model geometry. The stress  $\sigma_{xx}$  acting on the right boundary of the modeled (light red) domain  $\Omega$  comprises the lithostatic pressure of overburden ice  $p_i$  and a dynamic "far field" longitudinal stress contribution  $\sigma_i$ ;  $p_w$  denotes the hydrostatic pressure. The red mark represents the initially damaged area.

## 1.2.2 Governing Equations

While the deformation of ice is a thermo-mechanically coupled problem, we restrict ourselves in this work to a purely mechanical setting. Plugging in the assumed elastic rheology (1.8) and the definition of strain (1.7) into the balance of linear momentum (in the quasi-static approximation) (1.5), together with the incompressibility assumption (1.4) yields the following set of mechanical equations for the displacement  $\mathbf{u}$  and the effective pressure  $\bar{p}$  in the reference domain  $\Omega$

$$\nabla \cdot \left[ (1 - D) \frac{E}{(1 + \nu)} (\nabla \mathbf{u} + \nabla^T \mathbf{u}) \right] - \nabla [(1 - D) \bar{p}] - \nabla (D p_w) + \mathbf{b} = \mathbf{0}, \quad (1.16)$$

$$\nabla \cdot \mathbf{u} = 0, \quad (1.17)$$

with  $\Omega$  representing the block of ice (light red) illustrated in figure 1.1,  $\mathbf{b} = (0, \rho_i \cdot g)$  is the external body force vector, which in our case represents gravity. These equations (1.16 and 1.17) together with governing equation for the damage  $D$  (eq. 1.14) that describes the evolution of  $D$  in  $\Omega$

$$\dot{D} - \frac{1}{2} l_c^2 \Delta \dot{D} = \dot{D}_{loc}, \quad (1.18)$$

form a full set of governing equations describing the crevasse propagation model, where the damage source term  $\dot{D}_{\text{loc}}$  is given by eq. 1.9. Thus the process of finding the solution consists of solving the set of the governing equations (1.16, 1.17 and 1.18) for variables  $\bar{p}$  (the effective pressure),  $\mathbf{u}$  (the displacement vector field) and the damage  $D$ .

### 1.2.3 Initial and Boundary Conditions

To define the problem properly, it is essential to specify the conditions on the problem domain boundaries. There are two main types of boundary condition (BC) - Dirichlet BC (restricts the value of the solution itself at the boundary of the domain) and Neumann BC (specifies the value of the normal derivative of solution at the domain boundary). Alongside the boundary conditions, for time-dependent problems, it is necessary to specify also the initial condition (IC) to find the unique solution from the family of general solutions.

To simplify the considered problem, we suppose the ice slab to be freely floating in the underlying ocean, which we approximate by the so-called free-slip condition. This condition is applied on the bottom boundary, denoted as  $\Gamma_1$  in figure 1.1. The top edge of the ice slab, denoted as  $\Gamma_4$  is stress free, i.e., subjected to a homogeneous Neumann boundary condition. To avoid a free translation (a rigid body motion) of the whole glacier, we will also employ a free-slip along the left edge, which complies with the symmetry of the problem - this part of the boundary is denoted as  $\Gamma_2$  in figure 1.1. The right-hand side of the rectangular subdomain (denoted as  $\Gamma_3$  in figure 1.1) is subject to a horizontal stress condition represented by  $\sigma_{xx}$ . According to Weertman (1957) and Duddu et al. (2020), we can suppose the long wavelength approximation for an incompressible fluid, in which the horizontal Cauchy stress  $\sigma_{xx}$  is dependent on the depth linearly. Then  $\sigma_{xx}$  can be decomposed to a lithostatic  $p_i$  and a "far-field" dynamic stress  $\sigma_i$

$$\sigma_{xx}(d) = -p_i(d) + \sigma_i, \quad (1.19)$$

$$p_i(d) = \rho_i g d, \quad (1.20)$$

where  $d$  is the depth from the surface of the ice slab,  $g$  is the magnitude of gravity, and the far field tensile stress is given by Duddu et al. (2020, APPENDIX A, eq. A2)

$$\sigma_i = \frac{1}{2} \rho_i g H - \frac{1}{2} \frac{\rho_i^2}{\rho_w} g H, \quad (1.21)$$

where  $H$  is the height of the ice slab. Concerning damage  $D$ , we apply homogeneous Neumann boundary conditions on all boundaries.

The only variable involving explicit time derivative and thus requiring an initial condition is the damage  $D$ . The initial condition for the test case set the ice to be undamaged ( $D = 0$ ) on the whole rectangular subdomain, except for the square of tiny dimensions (relatively to the subdomain dimensions), where we consider the ice to be fully damaged ( $D = 1$ ).

### 1.2.4 The Overview of Physical Parameters

Material properties and other parameters appearing in the model formulation are listed in table 1.1. Additionally, we establish the maximum value of damage

$D_{\max}$  (that henceforth represents fully damaged ice) to prevent ill-conditioning that occurs for  $D = 1$ .

Table 1.1: The overview of physical parameters used for simulation of the damage propagation.

Parameter	Value	Units
$E$	$9.5 \times 10^9$	Pa
$\nu$	0.5	-
$\rho_i$	920	$\text{kg} \cdot \text{m}^{-3}$
$\rho_w$	1000	$\text{kg} \cdot \text{m}^{-3}$
$g$	9.81	$\text{m} \cdot \text{s}^{-2}$
$B$	$5.232 \times 10^{-7}$	$\text{MPa}^{-r} \cdot \text{s}^{-1}$
$r$	0.43	-
$\alpha$	0.21	-
$\beta$	0.63	-
$k_1$	-2.63	-
$k_2$	7.24	$\text{MPa}^{-1}$
$D_{\max}$	0.99	-
$l_c$	2.5 - 10	m

## 1.3 Numerical Implementation

Now that we have formulated the governing equations of our problem and set the idea of realization, we will get to the main principle behind the FEM and subsequently formulate the so-called weak formulation of our governing equations. Afterwards, we will suggest a specific FEM implementation using the FEniCS library.

### 1.3.1 The Finite Element Method

The finite element method (FEM) is a powerful, irreplaceable method for finding the numerical solution of initial- and boundary-value problems for partial differential equations (PDEs). It is widely used for complicated geometries and material properties where analytical solutions cannot be obtained. The FEM is employed extensively to analyze solids, fluids, structures, heat transfer, and basically in every field of engineering analysis that covers continuum mechanics.

The FEM is built on two fundamental attributes, which lie behind its successful usage and utility. At first, the FEM is based on the principle of bounded partitioning domains into several smaller, non-overlapping subdomains (the finite

elements). Functions over these finite elements are approximated by local functions, usually polynomials. Secondly, the initial- and boundary-value problems we apply this solving method on are formulated in a so-called weak (integral) form. Consequently, the contributions of each subdomain to the global integrals sum up to produce an integral characterizing the problem over the whole domain.

Formally, the weak formulation is found by multiplying the differential equation by a test function and integrating over the whole domain, while we integrate by parts via Green's theorem. The choice of the function spaces typically reflects both the structure of the PDE, as well as the (Dirichlet) boundary conditions - e.g., both the sought solution and the test function have to be zero at some part of the domain boundary. As a result, we get a differential equation with weaker conditions on the smoothness of solutions and test functions in the so-called weak form (Bathe, 2006).

### 1.3.2 Weak Formulation

According to the aforementioned, to be able to solve the problem numerically using the finite elements method (FEM), we need to formulate the problem in the so-called weak formulation. The equations 1.22 and 1.23 represent the weak formulation of the mechanical governing equations (1.16 and 1.17), while equation 1.24 represents the weak form of governing equation (1.18) for damage  $D$

$$\begin{aligned} & \int_{\Omega} (1 - D) \frac{E}{(1 + \nu)} \nabla \mathbf{w} : (\nabla \mathbf{u} + \nabla^T \mathbf{u}) \, d\mathbf{x} \\ & - \int_{\Omega} (1 - D) \nabla \cdot \mathbf{w} \bar{p} \, d\mathbf{x} - \int_{\Omega} \nabla \cdot \mathbf{w} (D p_w) \, d\mathbf{x} \\ & - \int_{\Omega} \mathbf{b} \cdot \mathbf{w} \, d\mathbf{x} = \mathbf{0} \quad \text{on } \Omega \end{aligned} \quad (1.22)$$

$$\int_{\Omega} q \nabla \cdot \mathbf{u} \, d\mathbf{x} = 0 \quad \text{on } \Omega, \quad (1.23)$$

$$\int_{\Omega} \dot{D} v \, d\mathbf{x} + \frac{1}{2} l_c^2 \int_{\Omega} \nabla \dot{D} \cdot \nabla v \, d\mathbf{x} - \int_{\Omega} \dot{D}^{\text{loc}} v \, d\mathbf{x} = 0 \quad \text{on } \Omega, \quad (1.24)$$

where  $\mathbf{w}$ ,  $q$ , and  $v$  are (arbitrary) test functions from suitably chosen function spaces.

### 1.3.3 FEniCS

Numerical implementation of the weak form of equations 1.22 - 1.24 was performed in a finite element open-source library package FEniCS (Alnaes et al., 2015).

Our implementation was written from scratch, but we follow closely the implementation of Duddu et al. (2020), in particular the delicate choices concerning finite element function spaces. The original code was implemented in FEniCS *v. 2016*, we rewrote it in FEniCS *v. 2019*.

We employed internal FEniCS meshing subroutines to generate the computational mesh according to geometry mentioned above (fig. 1.1), and replaced the initially damaged zone by a tiny notch (of the same size) in the domain geometry.

At first, we generate a mesh representing the modeling domain  $\Omega$  with the value of the mesh-resolution parameter set to 50. The rectangle area (symmet-

rically placed with respect to the notch representing the pre-damaged zone) of dimensions 40 m  $\times$  125 m of generated mesh is twice refined, and similarly located area (20 m  $\times$  125 m) is refined one more time. This should provide us with a better resolution of the crack propagation at the tip on one hand and save us some computing power and time on the other hand (compared to the whole domain having such mesh resolution).

Now, we are ready to present the finite element approximation of the problem 1.22 - 1.24. For the mechanical problem, we used Taylor-Hood elements (CG 2, CG 1) for  $(\mathbf{u}_h, \bar{p}_h)$ , the finite element approximations of  $(\mathbf{u}, \bar{p})$ . Here, "CG" denotes the Continuous Galerkin (the standard Lagrange family of piecewise polynomial elements), and the number determines a degree of polynomials. For the damage problem, we used a special class of so-called Quadrature elements (denoted as "Q") that allow to robustly deal with the nonlinearities and activation phenomena in the damage evolution. So the finite-element setting is as follows. At each time level  $k$ , we look for the triplet  $\mathbf{u}_h^k, \bar{p}_h^k, D_h^k \in \mathcal{U}(\text{CG } 2) \times \mathcal{P}(\text{CG } 1) \times \mathcal{D}(\text{Q})$ , such that

$$\begin{aligned} & \int_{\Omega_h} (1 - D_h^{k-1}) \frac{E}{(1 + \nu)} \nabla \mathbf{w}_h : (\nabla \mathbf{u}_h^k + \nabla^T \mathbf{u}_h^k) \, d\mathbf{x} \\ & - \int_{\Omega_h} (1 - D_h^{k-1}) \nabla \cdot \mathbf{w}_h \bar{p}_h^k \, d\mathbf{x} - \int_{\Omega_h} \nabla \cdot \mathbf{w}_h (D_h^{k-1} p_w^k) \, d\mathbf{x} \\ & - \int_{\Omega_h} \mathbf{b}_h^k \cdot \mathbf{w}_h \, d\mathbf{x} = \mathbf{0}, \end{aligned} \quad (1.25)$$

$$\int_{\Omega_h} q_h \nabla \cdot \mathbf{u}_h^k \, d\mathbf{x} = 0, \quad (1.26)$$

$$\int_{\Omega_h} \dot{D}_h^k v_h \, d\mathbf{x} + \frac{1}{2} l_c^2 \int_{\Omega_h} \nabla \dot{D}_h^k \cdot \nabla v_h \, d\mathbf{x} - \int_{\Omega_h} \dot{D}_h^{\text{loc } k} v_h \, d\mathbf{x} = 0, \quad (1.27)$$

for all  $(\mathbf{w}_h, q_h, v_h) \in \mathcal{U} \times \mathcal{P} \times \mathcal{D}$ . The symbol  $\Omega_h$  denotes the triangulation of the domain  $\Omega$ . The space  $\mathcal{U}$  is explicitly endowed with a homogeneous Dirichlet boundary condition for the normal component of vectors on the boundaries  $\Gamma_1$  and  $\Gamma_2$ , where the free-slip condition is prescribed. We use the notation  $A(t^k) \equiv A^k$ . In the FEM implementation of the problem, we used a decoupled procedure explicit in time. At each time step, we perform two computations - the first consists of solving the FEM implementation of the weak form of the mechanical problem (eq. 1.25 and 1.26), which provides us with the solution for the displacement  $\mathbf{u}$  and the effective pressure  $\bar{p}$ ; while the second provides us with the solution for the damage rate  $\dot{D}$  by solving the FEM implementation of the weak form of the governing equation for the damage  $D$  (eq. 1.27). Note that in the first computation, at time step  $t^k$ , the damage is hold constant with value from the previous time step from the second computation -  $D^{k-1}$ . Analogically, solutions for  $\mathbf{u}$  and  $\bar{p}$  from the first computation are used in the latter; however, computed at the same time step.

The solution of  $\dot{D}$  is used at each time step to update  $D$  directly in the corresponding degrees of freedom by

$$D^k = \min \{ \dot{D}^{k-1} \cdot dt + D^{k-1}, D_{\max} \}. \quad (1.28)$$

We used a uniform time step  $dt = 1.2$  months, which makes up 400 time steps for a forty-year long simulation.

The complete source code consisting of *the mesh generator* and *the main problem solver* for the FEniCS project simulation is attached to the electronic version of the thesis.

## 2. Numerical Experiments

In this section we provide results of a set of simulations of the top-crack propagation through an ice slab, designed to test the solution dependence on various model parameters and to compare the results quantitatively with the standard crack propagation theory in the framework of linear elastic fracture mechanics (LEFM) - see A.1.

All of the simulations were solved for a two-dimensional block of ice of dimensions  $500 \text{ m} \times 125 \text{ m}$ . However, all of the visual outputs are cropped to  $90 \text{ m} \times 90 \text{ m}$  (horizontally symmetrical and connected to the upper edge) squares for better comparison. All of the results were visualized using ParaView (Ahrens et al., 2005). The boundary and initial conditions together with the model parameters are those that have been specified in the previous section (1.2.3). The time period was set to 40 years with respect to "test simulations" that showed the convergence of the problem in approximately 35 years for time step  $dt = 1.2$  months, which we used as a default in all simulations. The initial stage of the crevasse is represented by the initially damaged area (IDA) - a square notch of width 2.5 m at default.

### 2.1 Water-free Crevasse Propagation and Sensitivity to Model Parameters

The first application of the model was the FEM simulations for the water-free crevasse, where we compare the effect of model parameters on the final shape of the crack. The parameters are listed in table 2.1, which also contains default values of the parameters. The first investigated parameter is a time step  $dt$ , which represents the time interval between two points in time, as we approximate the real continuous time by a finite number of discrete time steps. One can see that  $dt$  appears explicitly in the damage evolution (in eq. 1.28) and therefore can affect it. All performed simulations modeled the evolution over 40 years, therefore using default  $dt = 1.2$  months means 400 time steps per simulation, unless explicitly stated otherwise. The second studied model parameter is the length scale parameter  $l_c$  introduced in eq. 1.14 with estimated value 1.15 in publication A. Hillerborg et al. (1976). The  $l_c$  predicts the length of the crevasse propagation process zone ahead of the tip (Duddu et al., 2020). The third examined parameter, a mesh resolution, is arbitrary in the FEniCS environment. It changes the resolution of generated mesh in the FEM implementation, which directly changes the resolution of the output simultaneously with the computational costs. The fourth reviewed parameter is the width of damage active zone (WDAZ) that we have to employ to restrict the horizontal propagation of the damage from the crack tip to a finite size area (Duddu et al., 2020), in order to be consistent with the LEFM model - in simulations approximated by a strip of finite size. This is one of the weaker parts of the model, as the absence of such restriction would result in the disruption of the whole modeled domain because the whole top boundary is subject to tension, and the damage would gradually increase there (due to the absence of healing in the model). The last studied parameter

is the initially damaged area (IDA), which expresses the fully damaged ice at the beginning of the simulation - it serves as a part of the initial condition; thus, it directly affects the simulation. In the numerical implementation, we replaced the area (where  $D(0) = D_{\max}$ ) by the notch in the mesh geometry as mentioned above.

Table 2.1: The overview of model parameters used for simulation of the damage propagation.

Parameter	Default value
$dt$ (time step size)	1.2 months
$l_c$ (length scale parameter)	5 m
mesh resolution	50
the WDAZ (the width of damage active zone)	20 m
the IDA (the initially damaged area)	$2.5 \times 2.5 \text{ m}^2$

The effect of each of the parameters was examined with other parameters fixed at their default value. Figures 2.1 to 2.5 display the final state ( $t = 40$  years) of a top water-free crevasse for three different values of each parameter, the left-hand side of these figures also displays the mesh geometry. The damage  $D$  is on a logarithmic scale.

Figure 2.1 shows the crack evolution for different values of time step size -  $dt = 7.3$  days, 1.2 months and 6 months. Parameter  $dt$  does not seem to have a visible impact on crevasse propagation - regarding the shape or size of the final stage.

Figure 2.2 shows the crack evolution for different values of the length scale parameter -  $l_c = 2.5$  m, 5 m and 10 m. Parameter  $l_c$  clearly affects both-the shape and size of final stage of the crevasse. As expected from the character of  $l_c$  parameter, the greater the parameter gets, the larger is the damaged area. Note that for smaller value of the parameter, we can see the change of the shape to the rectangular-like (compared to the circle-like for greater values).

Figure 2.3 shows the crack evolution for different values of the arbitrary mesh resolution parameter - mesh resolution = 25, 50 and 100. A mesh resolution does not seem to have the qualitative difference on the final crack stage that corresponds with the CPDM model - it should reduce the mesh size sensitivity for appropriately selected  $l_c$ ; yet, naturally, we can observe the difference in the smoothness of the damage.

Figure 2.4 shows the crack evolution for different values of the width of damage active zone - WDAZ = 10 m, 20 m and 40 m. The width of damage active zone influences the width of the final shape, which is the direct consequence of the definition of such parameter as it restricts the horizontal damage propagation at the crack tip to selected area. Therefore the WDAZ parameter has an important effect on the final crevasse shape.

Figure 2.5 shows the crack evolution for different values of the initially damaged area - IDA =  $1.25 \times 1.25 \text{ m}^2$ ,  $2.5 \times 2.5 \text{ m}^2$  and  $5 \times 5 \text{ m}^2$ . The size of the

initially damaged area clearly affects the final depth of shallow crevasse (what originates from the change of the geometry), however, one might expect this effect to vanish for deep crevasses - e.g., cases with higher tensile stress.

To sum up, parameters  $l_c$  and the WDAZ have the most notable effect on the water-free crevasse propagation, together with the IDA parameter having a substantial effect only for shallow crevasses. The effect of parameters  $dt$  and the mesh resolution on the model sensitivity is almost none (considered the smoothness for the finest mesh did not change the size or shape of the crevasse).

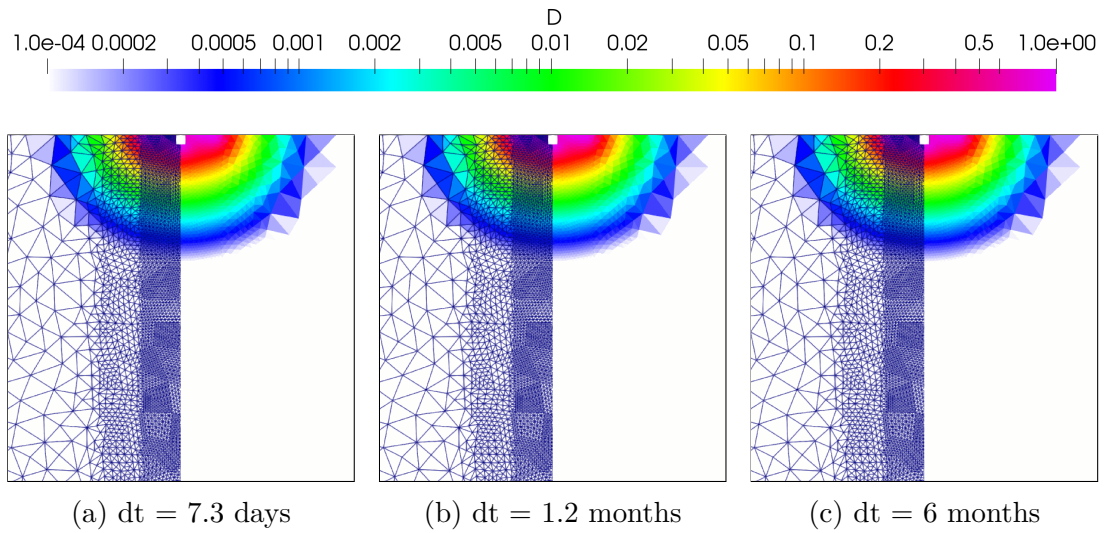


Figure 2.1: The effect of time step  $dt$  size on crevasse propagation.

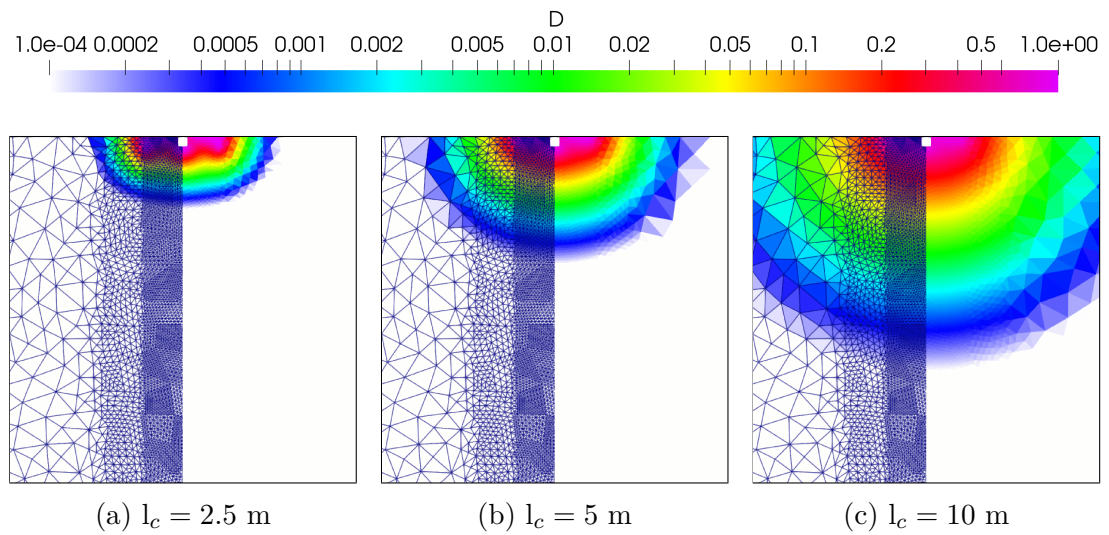


Figure 2.2: The effect of  $l_c$  parameter on crevasse propagation.

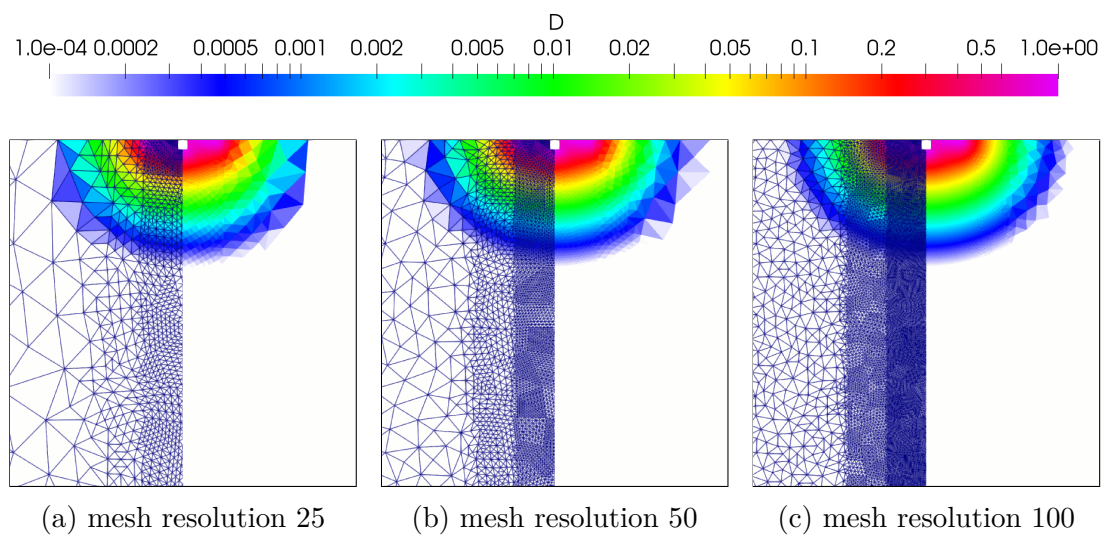


Figure 2.3: The effect of a mesh resolution on crevasse propagation.

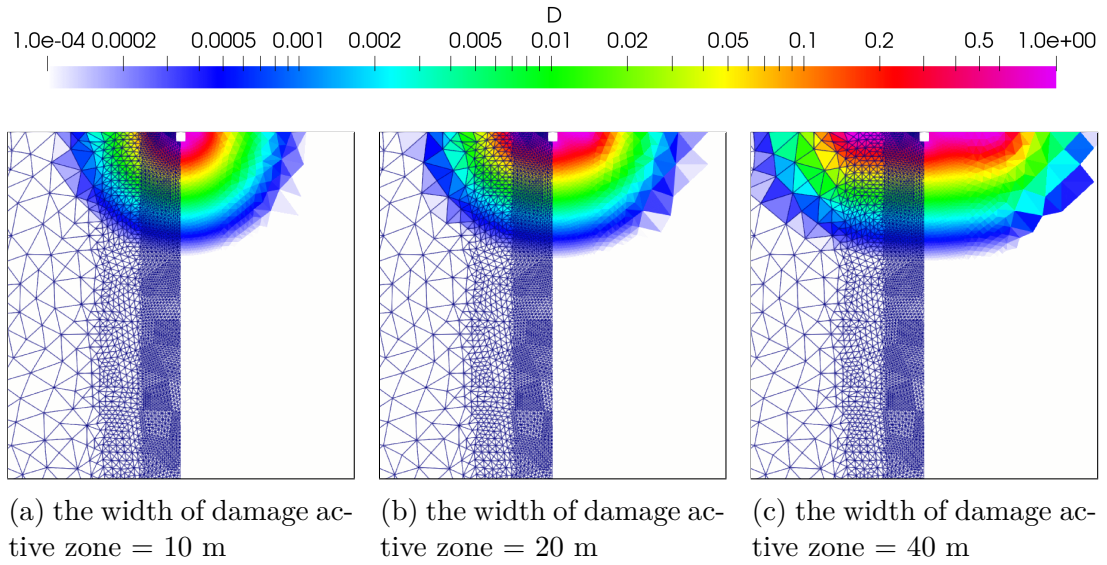


Figure 2.4: The effect of the width of damage active zone on crevasse propagation.

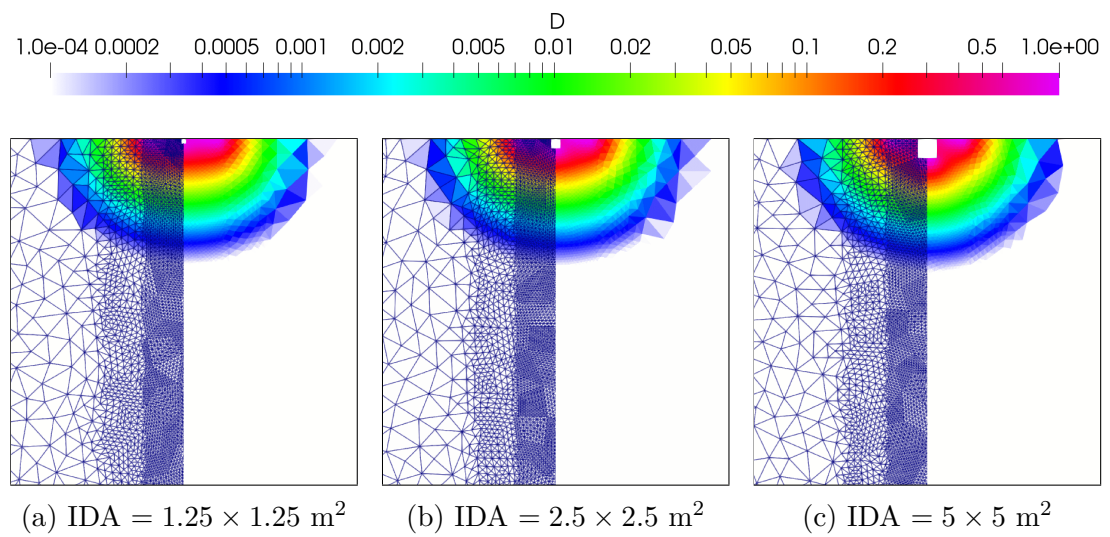


Figure 2.5: The effect of the initially damaged area on crevasse propagation.

## 2.2 The Dependence of the Water-free Crevasse Depth on Model Parameters

We also examine the evolution of crack depth and its dependence on the same set of model parameters as above (2.1). The effect of such parameters on time evolution of the crevasse depth can be seen in figures 2.6 to 2.10. However, the crack depth in the considered model has to be defined in terms of a selected damage value threshold for  $D$  (looking for the position of the lowermost point of selected iso-contour) - we consider values  $D = 0.5, 0.6, 0.7, 0.8$  and  $0.9$ .

Figure 2.6 shows the crack depth evolution for different values of time step size -  $dt = 7.3$  days, 1.2 months and 6 months. The size of  $dt$  has a relatively small, but noticeable effect on smoothness of the depth evolution (mainly in early stages of the crack propagation). However, one can see by comparing 2.6a and 2.6b that we do not observe "jump" in the depth evolution of  $D = 0.9$  for small  $dt$ , which can be interpreted by having sufficient time resolution time steps to cover the initial sudden phase of the crack propagation. On the other hand, it seems that for greater time steps (than default) we do not observe significant changes in depth evolution, but could expect a loss of accuracy and potential instabilities for very large time steps (with respect to simulated time period).

Figure 2.7 shows the crack depth evolution for different values of the length scale parameter -  $l_c = 2.5$  m, 5 m and 10 m. Observations indicates that  $l_c$  has an impact on the speed of a damage propagation and its distribution across the space - for smaller  $l_c$  we notice the propagation of all selected damage iso-contours has relatively unified profile, while for greater  $l_c$  values selected damage iso-contours pull back from each other and more damaged areas occur much later. The distribution across space affects also the depth of the crevasse - one can see deeper penetration for  $D = 0.5$ , but more shallow penetration for  $D = 0.8$  (or absence of  $D = 0.9$ ) for greater  $l_c$ .

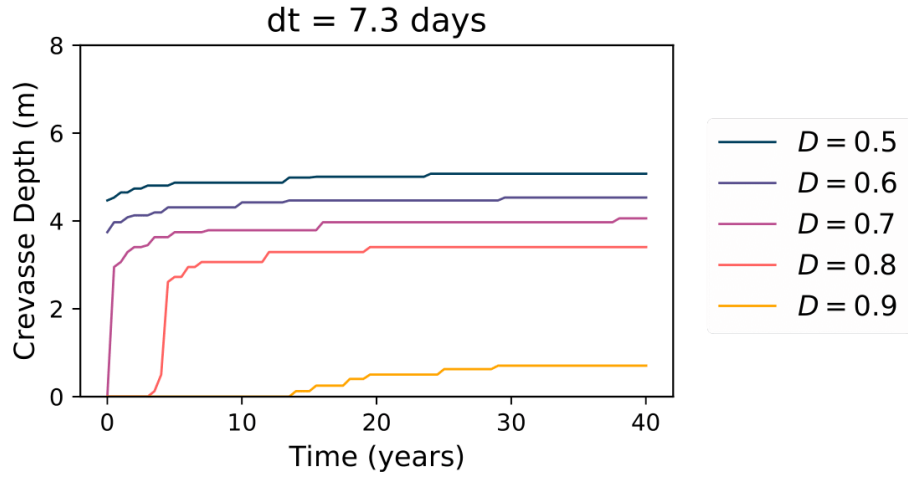
Figure 2.8 shows the crack depth evolution for different values of the arbitrary mesh resolution parameter - mesh resolution = 25, 50 and 100. For mesh resolution changes, we do not observe significant changes in the crevasse depth trends, which should be one of the main features of using the CPDM model. However, some smoothness fluctuations occur between individual cases as the fine (rough) structure provides more (less) points for the depth investigation (as we look for the lowermost point of selected damage iso-contour).

Figure 2.9 shows the crack depth evolution for different values of the width of damage active zone - WDAZ = 10 m, 20 m and 40 m. The dependence of crack depth on the WDAZ seems to be influenced only in the sense of the rate of the penetration (the slower penetration for the larger the WDAZ as the damage spreads over a larger area, this effect is significant mainly for damage values close to  $D_{\max}$ ).

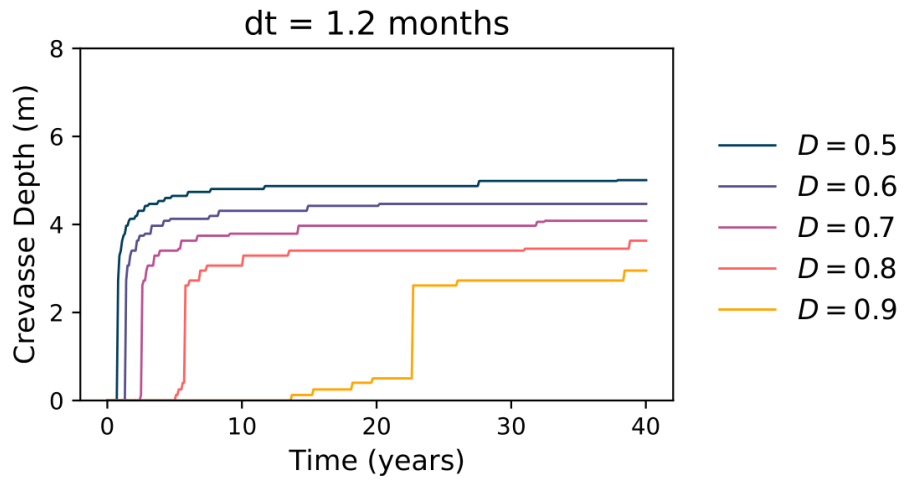
Figure 2.10 shows the crack depth evolution for different values of the initially damaged area - IDA =  $1.25 \times 1.25$  m<sup>2</sup>,  $2.5 \times 2.5$  m<sup>2</sup> and  $5 \times 5$  m<sup>2</sup>. The size of initially damaged area play significant role in the depth investigation of shallow crevasses. The primary reason of such behaviour is the size of studied case - for IDA =  $5 \times 5$  m<sup>2</sup>, the size of IDA is almost the size of the final depth for the default IDA size case. Thus, one can see that the depth of shallow crevasse strongly depends on the size of the IDA - for instance the ratio of final depth for

the  $IDA = 5 \times 5$  and  $IDA = 1.25 \times 1.25 \text{ m}^2$  is 1.76 ( $D = 0.5$ ) and 4.20 ( $D = 0.9$ ).

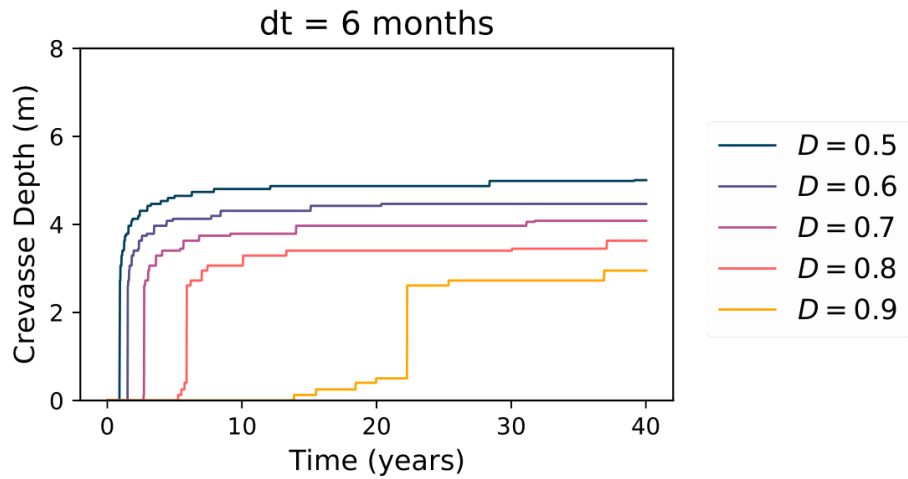
To conclude, the parameters with the most significant effect on the crevasse's final depth are  $l_c$  and the IDA, with  $dt$  and the WDAZ having a small effect, and the mesh resolution having almost none.



(a) The evolution of the depth of water-free crevasse for a time step  $dt = 7.3$  days.

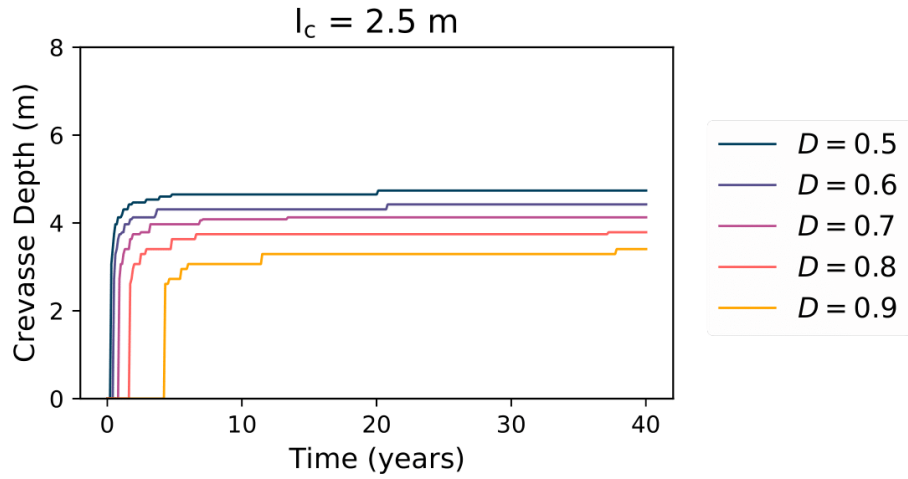


(b) The evolution of the depth of water-free crevasse for a time step  $dt = 1.2$  months.

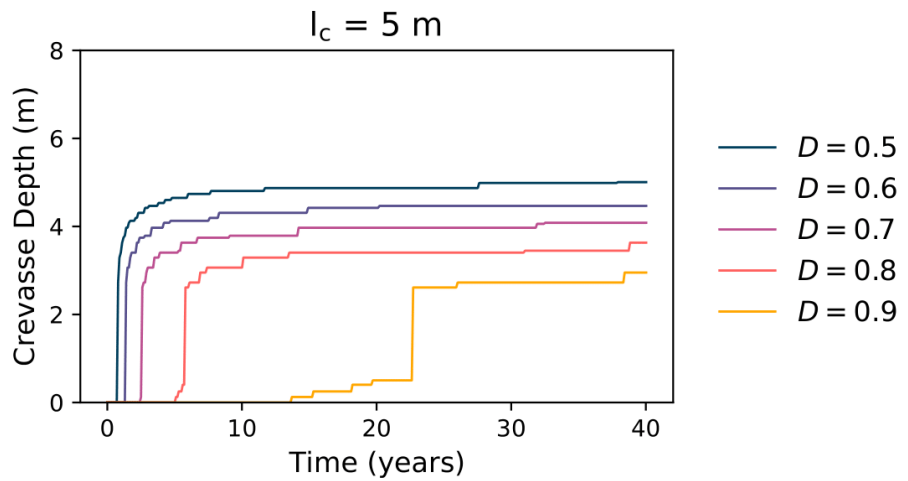


(c) The evolution of the depth of water-free crevasse for a time step  $dt = 6$  months.

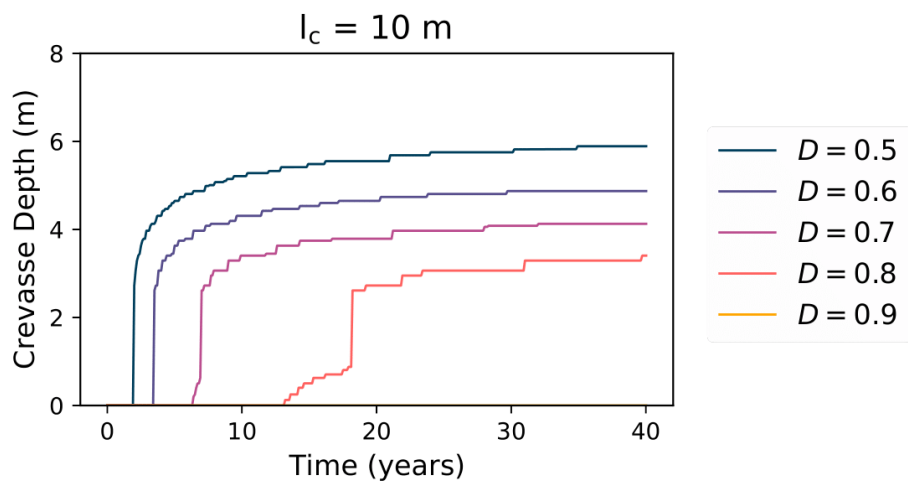
Figure 2.6: The comparison of the evolution of the depth of water-free crevasse with respect to the time step  $dt$  size.



(a) The evolution of the depth of water-free crevasse for the length scale parameter  $l_c = 2.5$  m.

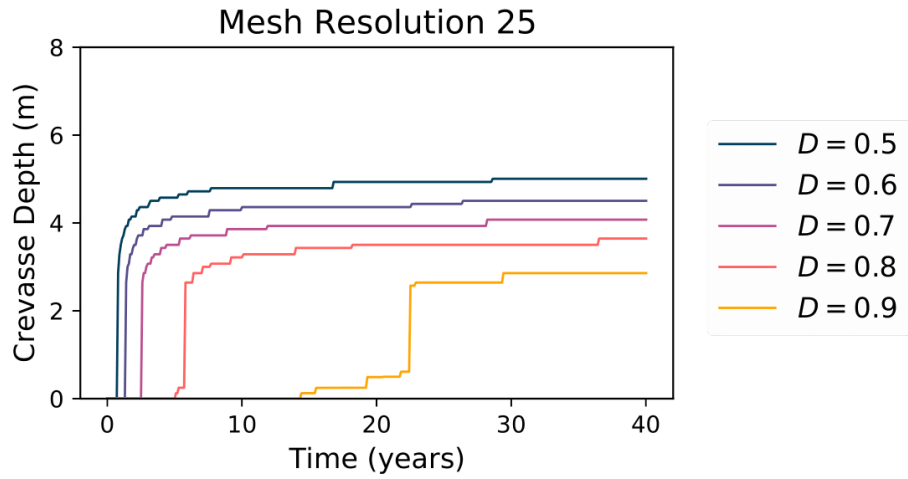


(b) The evolution of the depth of water-free crevasse for the length scale parameter  $l_c = 5$  m.

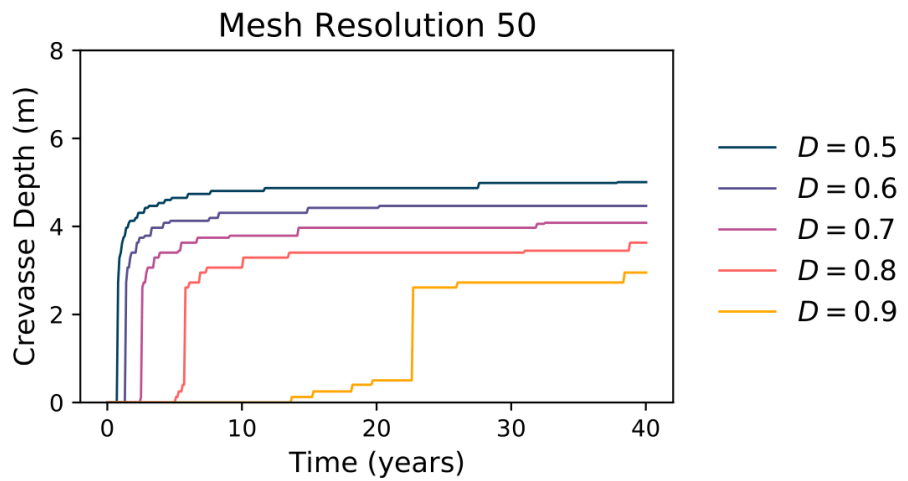


(c) The evolution of the depth of water-free crevasse for the length scale parameter  $l_c = 10$  m.

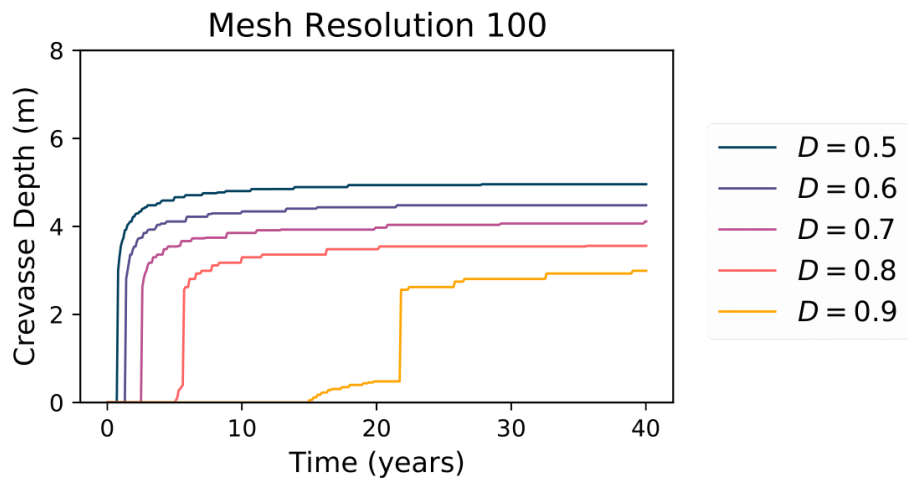
Figure 2.7: The comparison of the evolution of the depth of water-free crevasse with respect to the length scale parameter  $l_c$ .



(a) Mesh resolution 25.

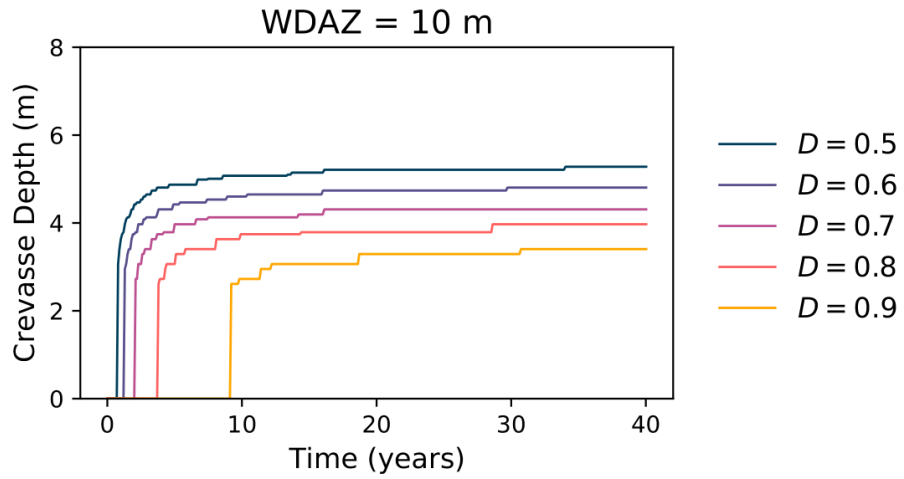


(b) Mesh resolution 50.

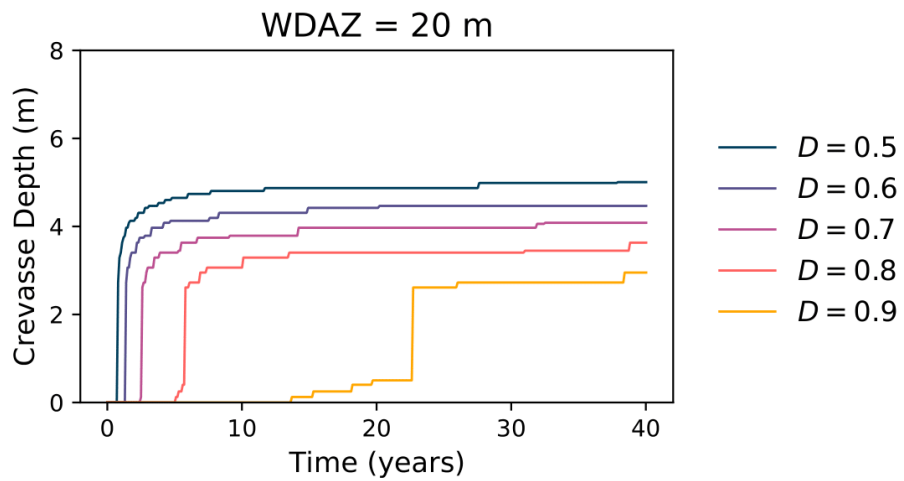


(c) Mesh resolution 100.

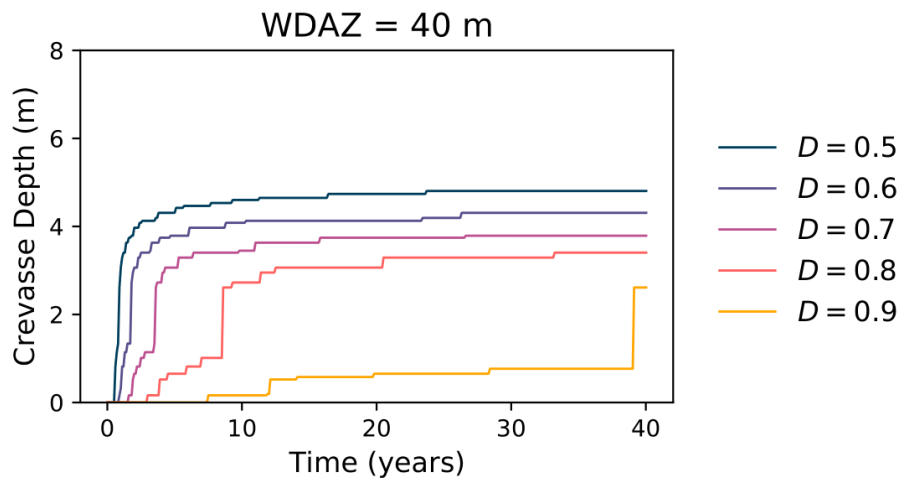
Figure 2.8: The comparison of the evolution of the depth of water-free crevasse with respect to the mesh resolution.



(a) The width of damage active zone = 10 m.

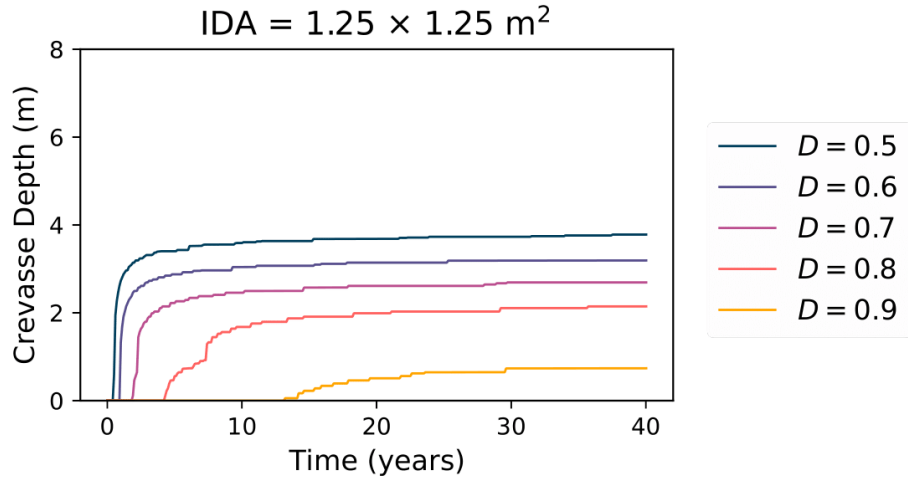


(b) The width of damage active zone = 20 m.

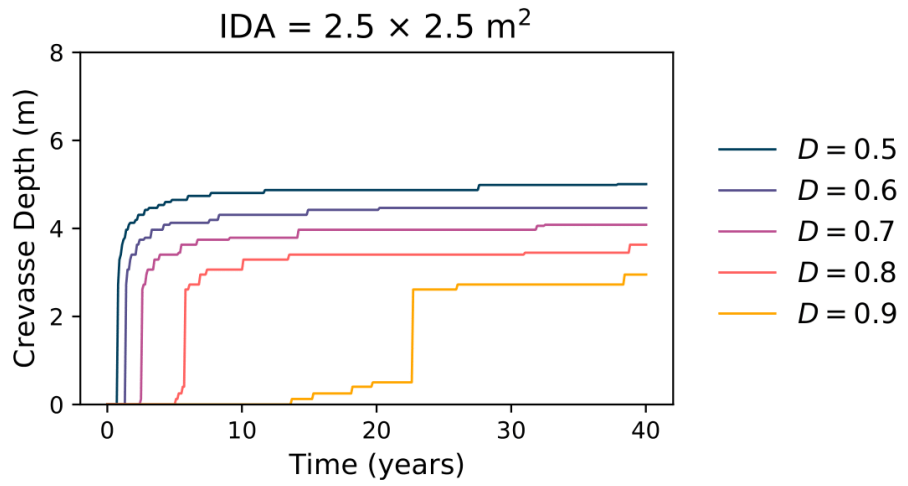


(c) The width of damage active zone = 40 m.

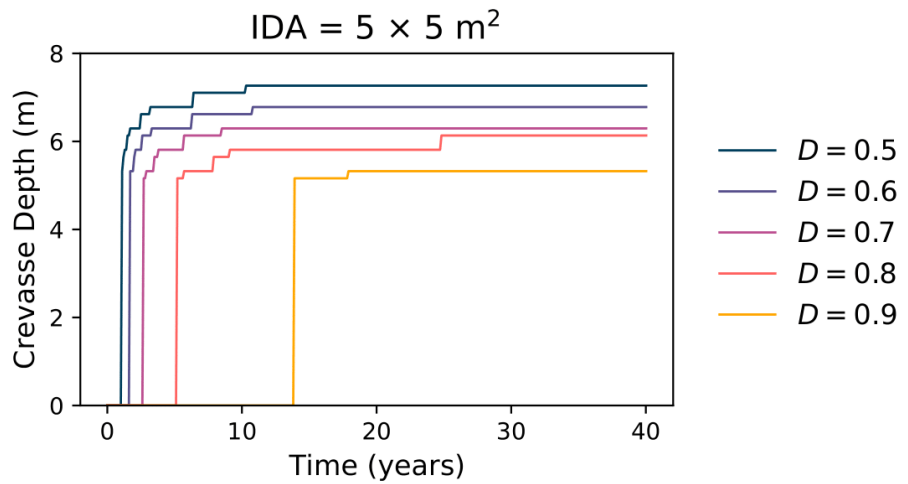
Figure 2.9: The comparison of the evolution of the depth of water-free crevasse with respect to the width of damage active zone.



(a) The initially damaged area =  $1.25 \times 1.25 \text{ m}^2$ .



(b) The initially damaged area =  $2.5 \times 2.5 \text{ m}^2$ .



(c) The initially damaged area =  $5 \times 5 \text{ m}^2$ .

Figure 2.10: The comparison of the evolution of the depth of water-free crevasse with respect to the size of the initially damaged area.

## 2.3 The Effect of Applied Longitudinal Stress

We explore how the crack propagation depends on the applied stress on the right boundary. We compare the default simulation ( $\sigma_{xx}$  given by 1.19), with a case, where we apply the additional tensile (depth independent) stress of magnitude  $\sigma_+ = 314\,000$  Pa; and juxtapose both cases with the theoretical expectations based on the LEFM by Weertman (1973).

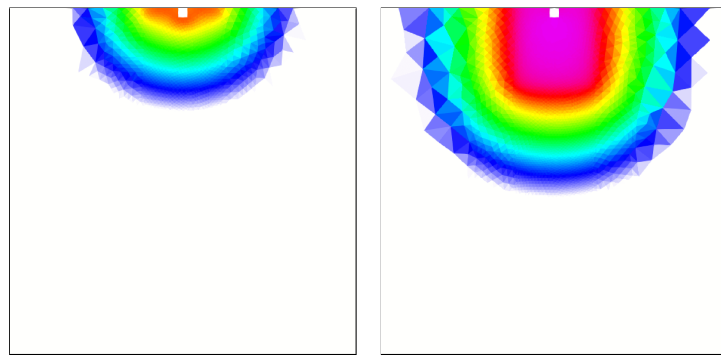
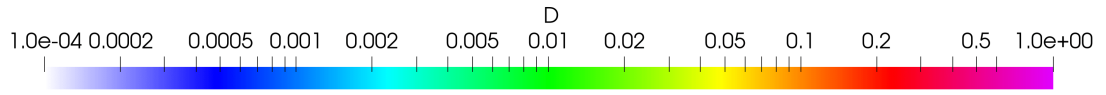
### 2.3.1 The Damage and the Crevasse Depth Evolution

Working with the additional tensile stress provides us with "more visible" outputs and enables us to compare the numerical results with the theoretical expectations for another state. Figure 2.11 shows the comparison of the time evolution of two water-free cracks - the default simulation with tensile stress  $\sigma_{xx}$  (left column) and the simulation with additional tensile stress  $\sigma_+$  applied (right column). We selected the time snapshots that cover the visual evolution stages rather than have a uniform time step between each other. As expected, the fastest crack propagation occurs at the beginning of the simulation (due to the increasing compressive overburden pressure with crack depth). The damage ( $D$ ) is displayed in a logarithmic scale. For better clarity we plotted the depth as a function of time as can be seen in figure 2.12, where we also compare it with theoretical expectations (see below).

According to Weertman (1973), the maximal penetration depth of a top water-free crack  $L_{\max}^{\text{top}}$  in a free-floating glacier is given by

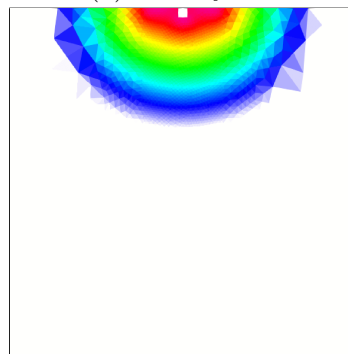
$$L_{\max}^{\text{top}} = \frac{\pi}{2\rho_i g} \sigma_{xx}, \quad (2.1)$$

where  $\sigma_{xx}$  is the tensile stress, which appears within the ice block. Considered the values of physical parameters (table 1.1), and the case with additional tensile stress  $\sigma_+$  applied, using eq. 2.1 we get the values listed in table 2.2 (denoted as Theoretical). Table 2.2 also contains values obtained by the FEM, for each of selected iso-contours ( $D = 0.5 - 0.9$ ). It is necessary to note that while the theoretical value of the depth for  $\sigma_{xx}$  was computed, in the case with additional tensile stress  $\sigma_+$  applied, we demanded the depth to be  $\frac{H}{2} = 62.5$  m - therefore the magnitude of increment to default  $\sigma_{xx}$  longitudinal tensile stress is (according to 2.1 and 1.19)  $\sigma_+ = 314\,000$  Pa.

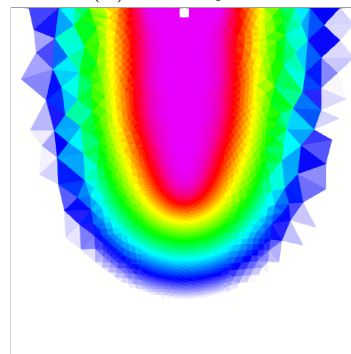


(a)  $t = 0$  years

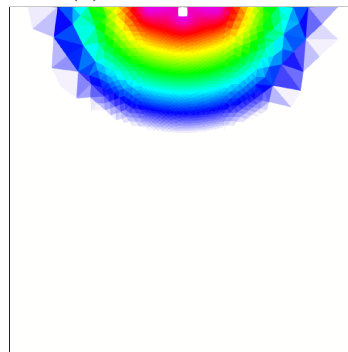
(b)  $t = 0$  years



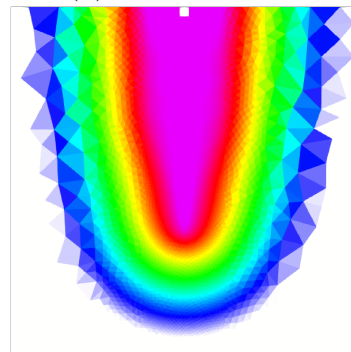
(c)  $t = 10$  months



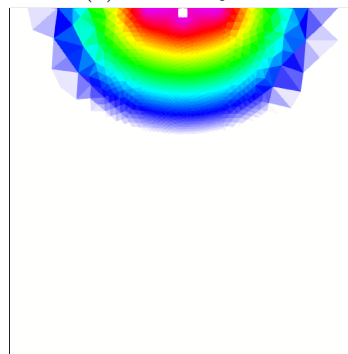
(d)  $t = 10$  months



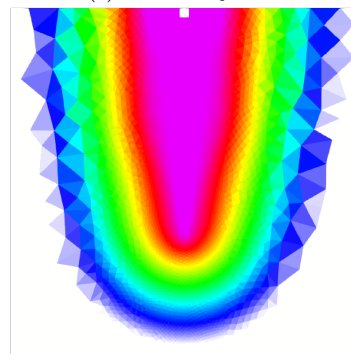
(e)  $t = 13$  years



(f)  $t = 13$  years



(g)  $t = 32.5$  years



(h)  $t = 32.5$  years

Figure 2.11: The crevasse evolution of two different tensile stress cases -  $\sigma_{xx}$  (left column) and  $\sigma_{xx} + \sigma_+$  (right column).

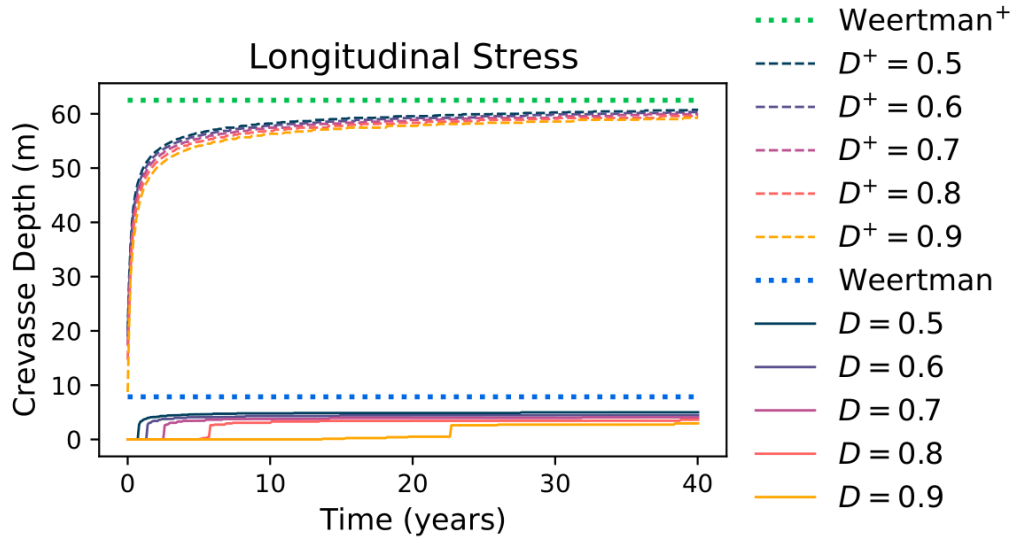


Figure 2.12: The crevasse depth evolution of two different tensile stress cases -  $\sigma_{xx}$  and  $\sigma_{xx} + \sigma_+$ .

Figure 2.12 shows the evolution of crevasse depth for water-free crevasses with the default values of model parameters (tab. 2.1). Damage levels  $D$  mark the case with standard tensile stress  $\sigma_{xx}$  and *Weertman* describes the theoretical maximal depth that crevasse should reach, considering the eq. 2.1. Damage levels  $D^+$  mark the case with additional tensile stress  $\sigma_+$  applied, *Weertman*<sup>+</sup> describes the theoretical maximal depth that crevasse should reach, considered the respective case. It can be seen that depth predictions by the damage based model have a relatively good quantitative agreement with the theoretical predictions based on the linear elastic fracture mechanics (LEFM). The relative error is 2.9 – 5.1% (depends on selected damage value) for the case with additional tensile stress applied. On the other hand, for the shallow crack, the relative error in crack depth is pretty significant, reaching up to 37 – 62%.

Table 2.2: The depth comparison of the theoretical prediction with the FEM results for top water-free crevasses.

	Theoretical	FEM				
Tensile stress		$D = 0.5$	$D = 0.6$	$D = 0.7$	$D = 0.8$	$D = 0.9$
$\sigma_{xx}$	7.9 m	5.0 m	4.5 m	4.1 m	3.6 m	3.0 m
$\sigma_{xx} + \sigma_+$	62.5 m	60.7 m	60.3 m	59.9 m	59.6 m	59.3 m

### 2.3.2 The Evolution of Other Model Relevant Physical Quantities

To provide a more complete picture, in this subsection, we document the evolution of all relevant physical quantities in the simulation with applied additional tensile stress  $\sigma_+$  (mentioned at the beginning of section 2.3). The studied case is the top water-free crevasse. The evolution of all considered quantities is shown in 6 snapshots distributed through the investigated time period unevenly ( $t = 70$  days, 130 days, 190 days, 315 days, 2.5 years and 40 years) to capture the evolution more precisely.

Figure 2.13 shows the time evolution of the damage  $D$  that propagates as expected concerning the examples above.

Figure 2.14 displays the evolution of the damage rate  $\dot{D}$ ; one can see that the area of the fastest damage rate is the largest at the beginning of the simulation and progressively concentrates at the tip as the crack propagates deeper.

Figure 2.15 displays the evolution of the local damage increment  $\dot{D}^{loc} \cdot dt$ , which again concentrates at the tip and gradually disappears as reaching the crevasse's final depth.

Figures 2.16 to 2.22 display the evolution of (in order): the effective maximum principal stress  $\bar{\sigma}^{(I)}$ , the effective von Mises stress  $\bar{\sigma}^v$ , the effective Hayhurst stress  $\bar{\chi}$ , the effective pressure  $\bar{p}$  and components of the effective Cauchy stress tensor -  $\bar{\sigma}_{xx}$ ,  $\bar{\sigma}_{xy}$ ,  $\bar{\sigma}_{yy}$ . We will briefly comment only on the effective Hayhurst stress  $\bar{\chi}$  as it depends on the other mentioned quantities - note that in fig. 2.18a (at the beginning of the simulation)  $\bar{\chi}$  concentrates below the IDA, while in fig. 2.18f  $\bar{\chi}$  goes to negative values, what causes the crack propagation to stop.

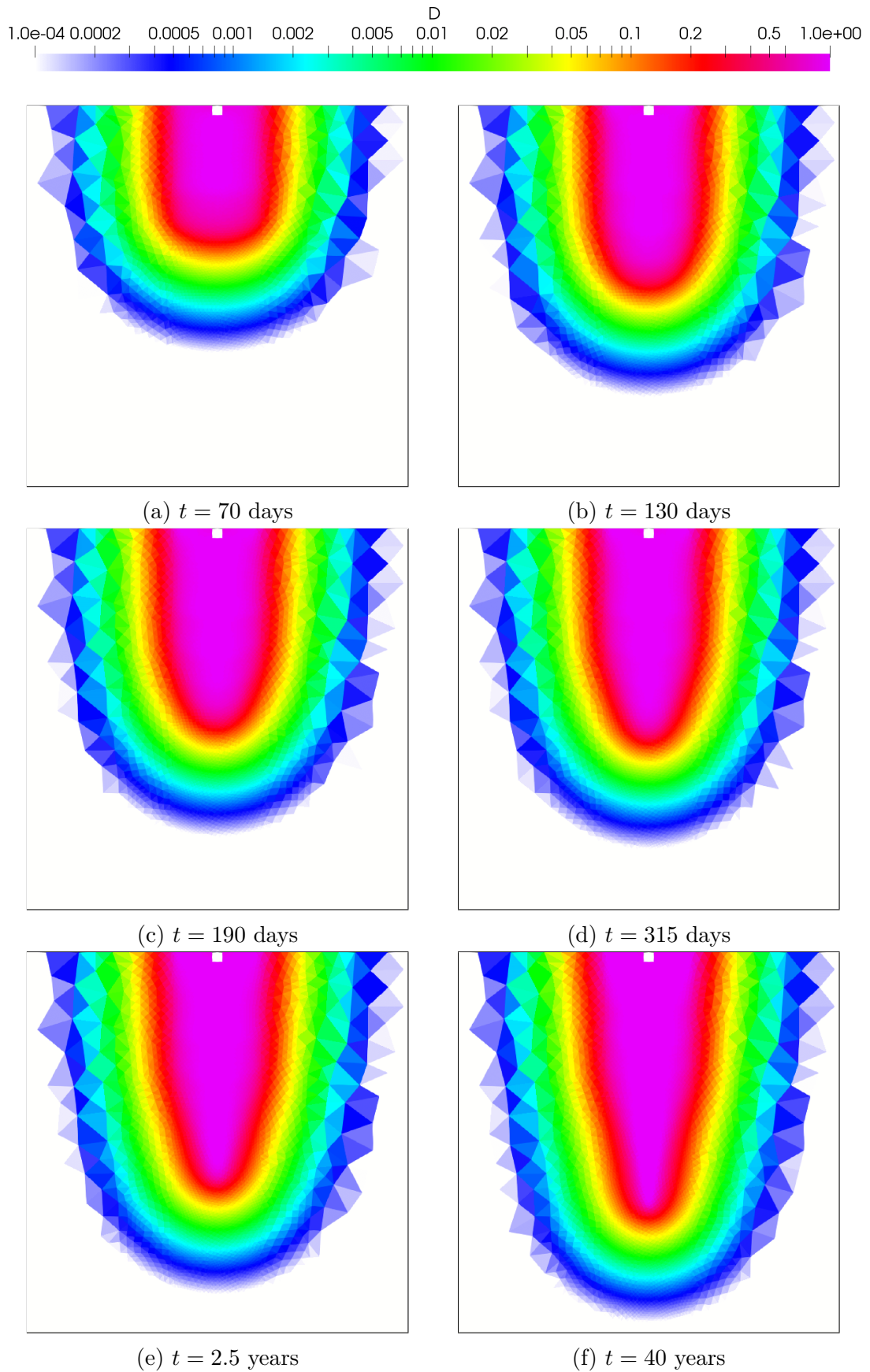


Figure 2.13: The evolution of the damage  $D$  quantity of the water-free crevasse propagation with default parameter values and increased longitudinal stress. The damage  $D$  quantity is displayed in a logarithmic scale.

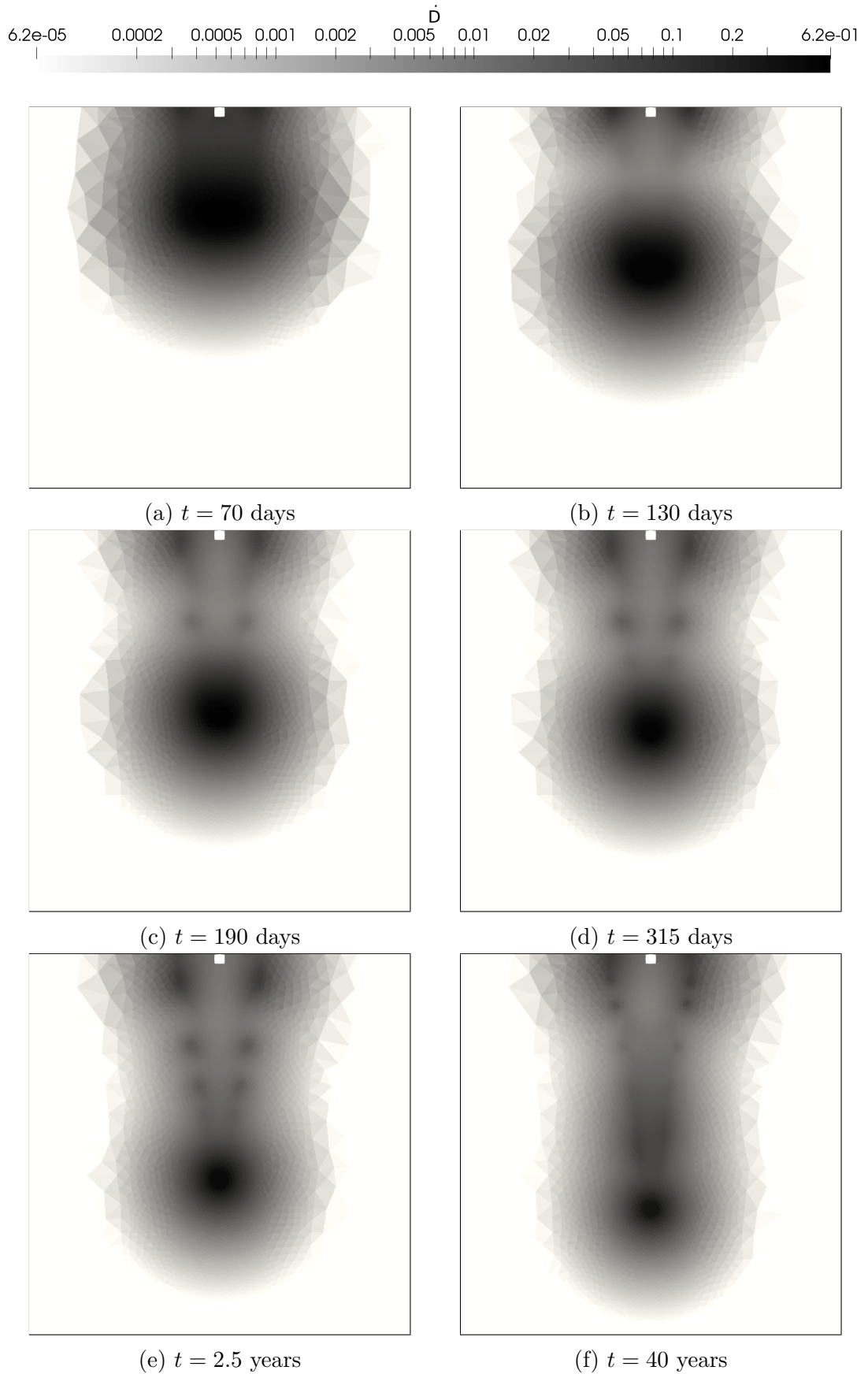


Figure 2.14: The evolution of the damage rate  $\dot{D}$  of the water-free crevasse propagation with default parameter values and increased longitudinal stress. The damage rate  $\dot{D}$  is displayed in a logarithmic scale.

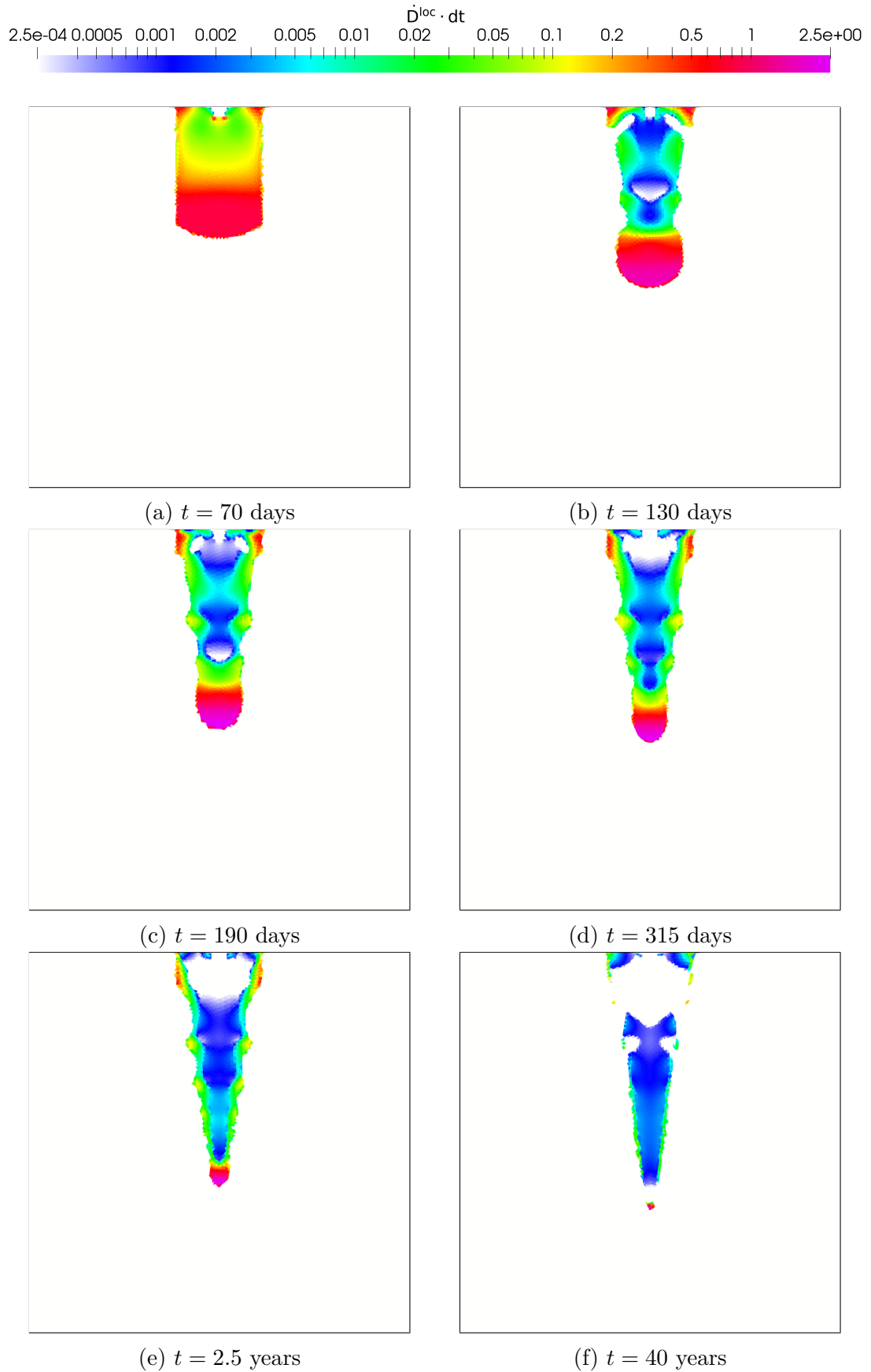


Figure 2.15: The evolution of the local damage increment  $\dot{D}^{loc} \cdot dt$  of the water-free crevasse propagation with default parameter values and increased longitudinal stress. The local damage increment  $\dot{D}^{loc} \cdot dt$  is displayed in a logarithmic scale.

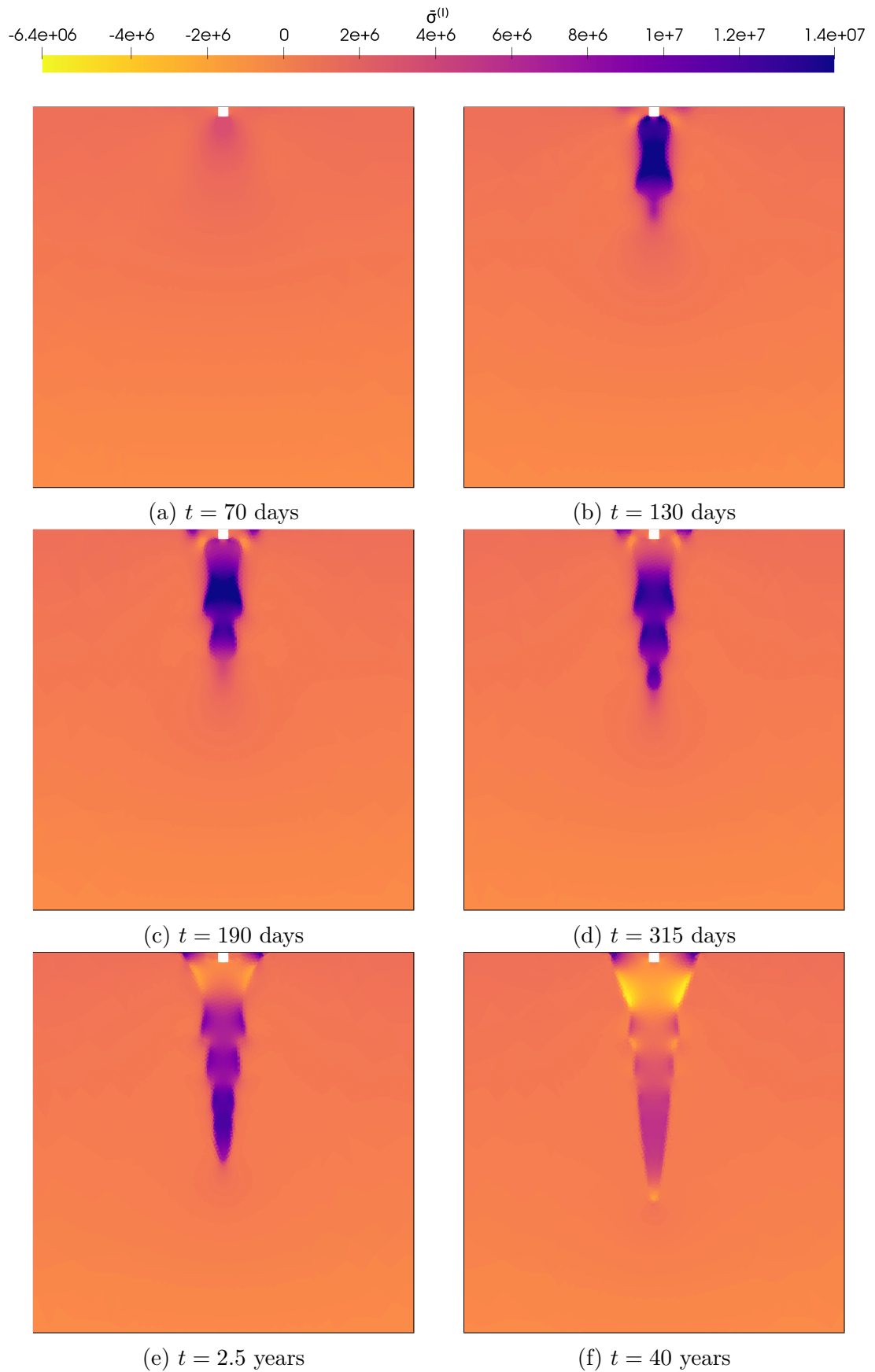


Figure 2.16: The evolution of the effective maximum principal stress  $\bar{\sigma}^{(I)}$  of the water-free crevasse propagation with default parameter values and increased longitudinal stress.

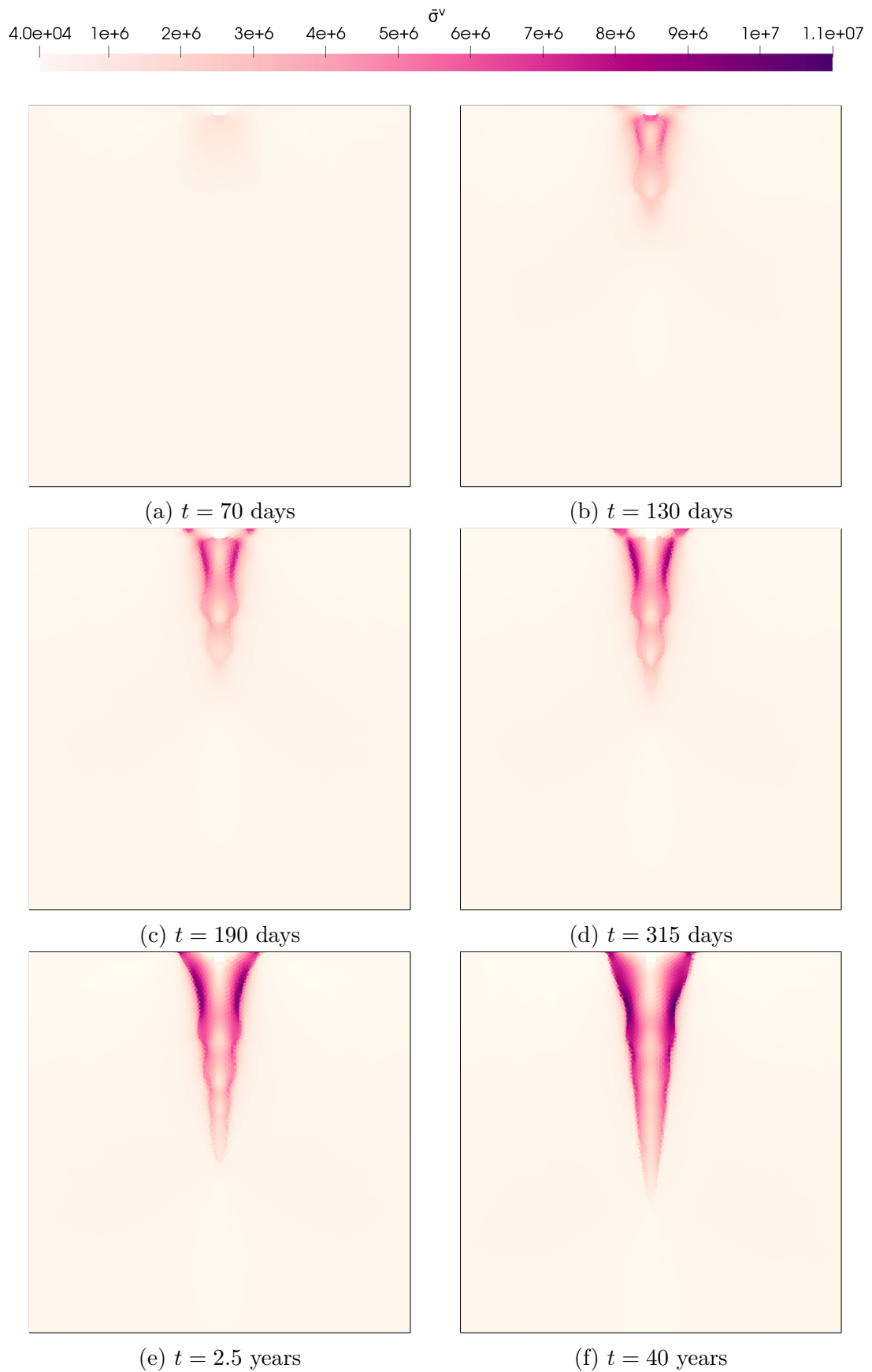


Figure 2.17: The evolution of the effective von Mises stress  $\bar{\sigma}^v$  of the water-free crevasse propagation with default parameter values and increased longitudinal stress.

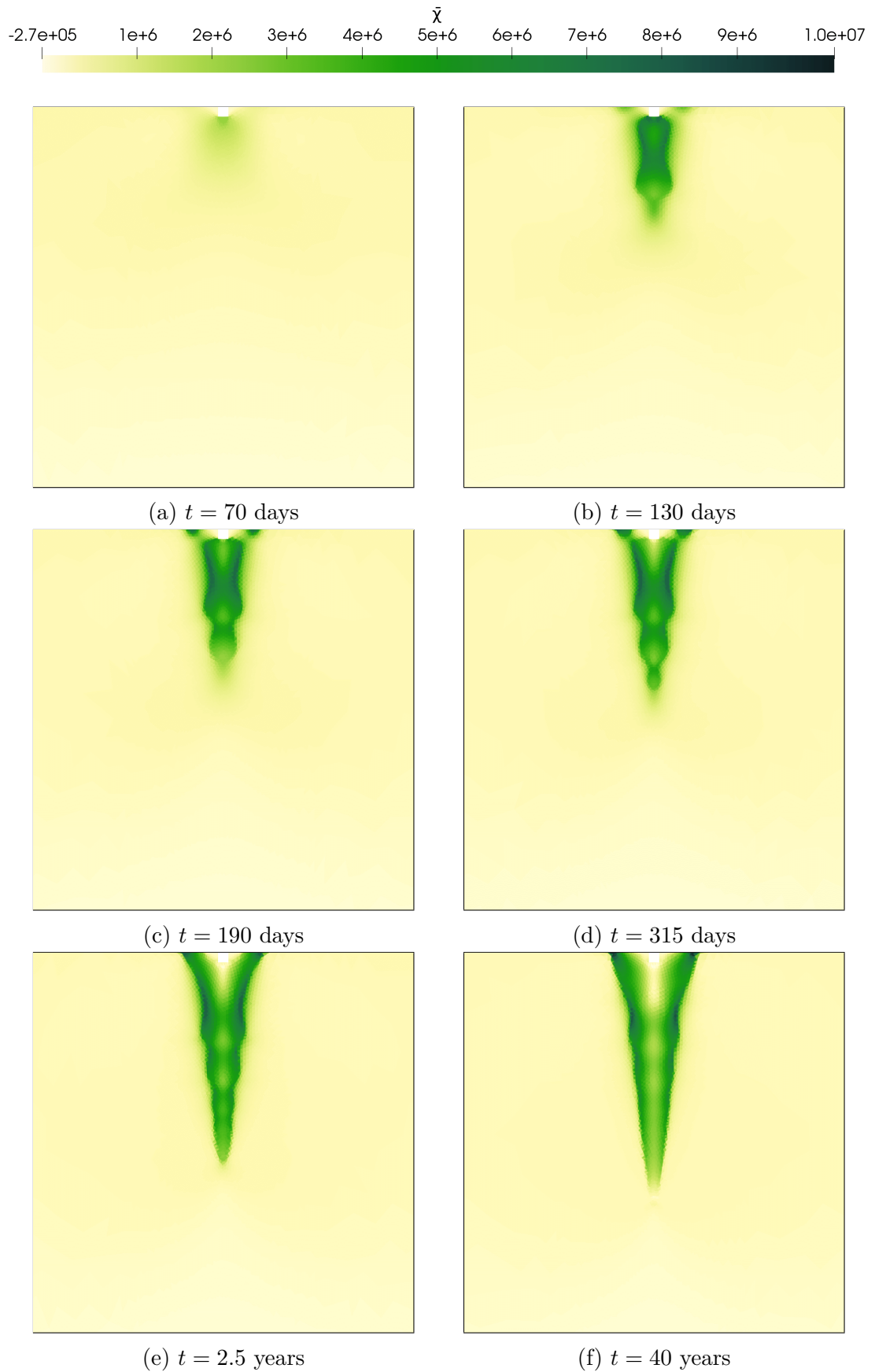


Figure 2.18: The evolution of the effective Hayhurst stress  $\bar{\chi}$  of the water-free crevasse propagation with default parameter values and increased longitudinal stress.

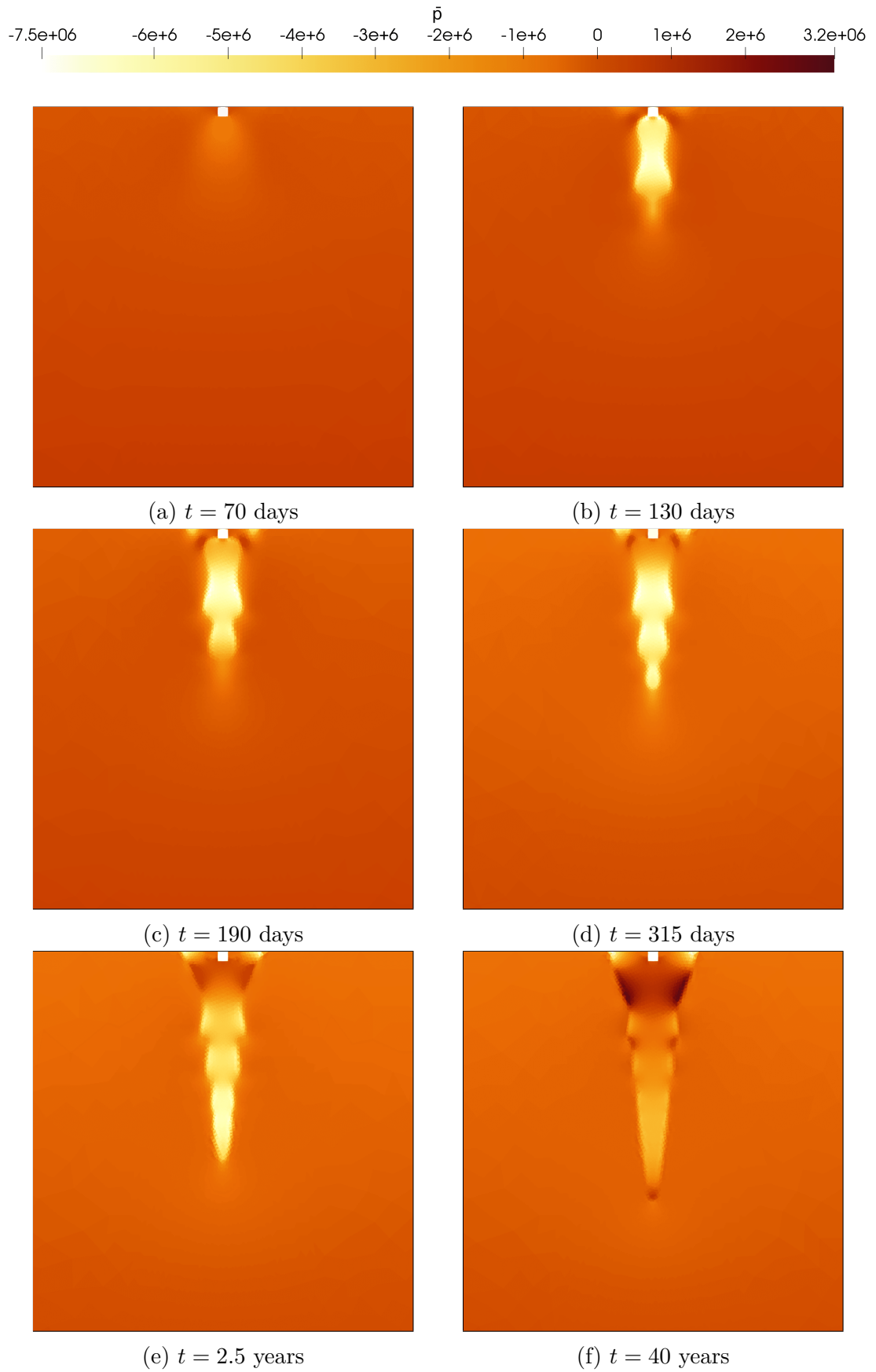


Figure 2.19: The evolution of the effective pressure  $\bar{p}$  of the water-free crevasse propagation with default parameter values and increased longitudinal stress.

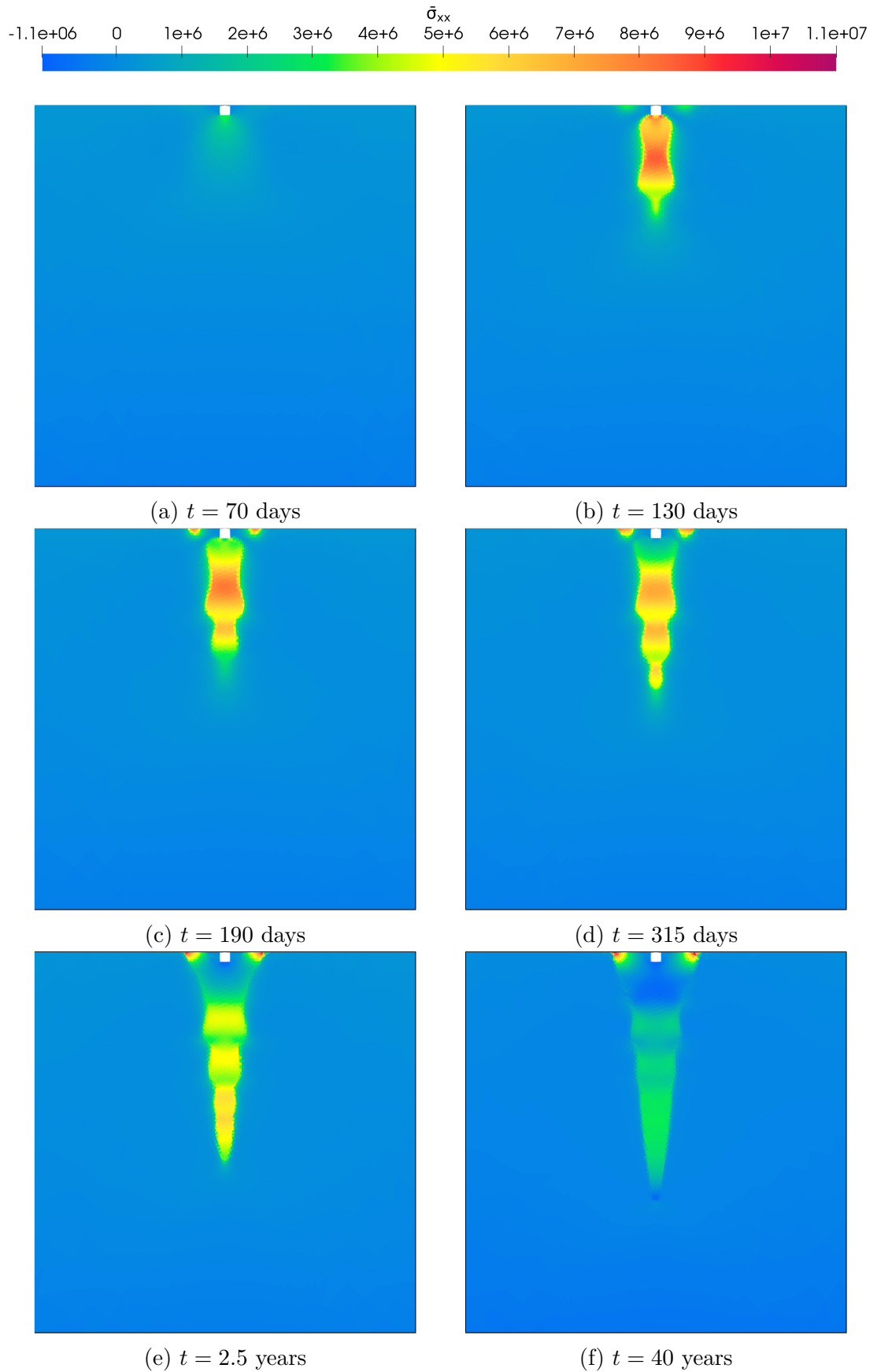


Figure 2.20: The evolution of the  $\bar{\sigma}_{xx}$  component of the effective Cauchy stress tensor, of the water-free crevasse propagation with default parameter values and increased longitudinal stress.

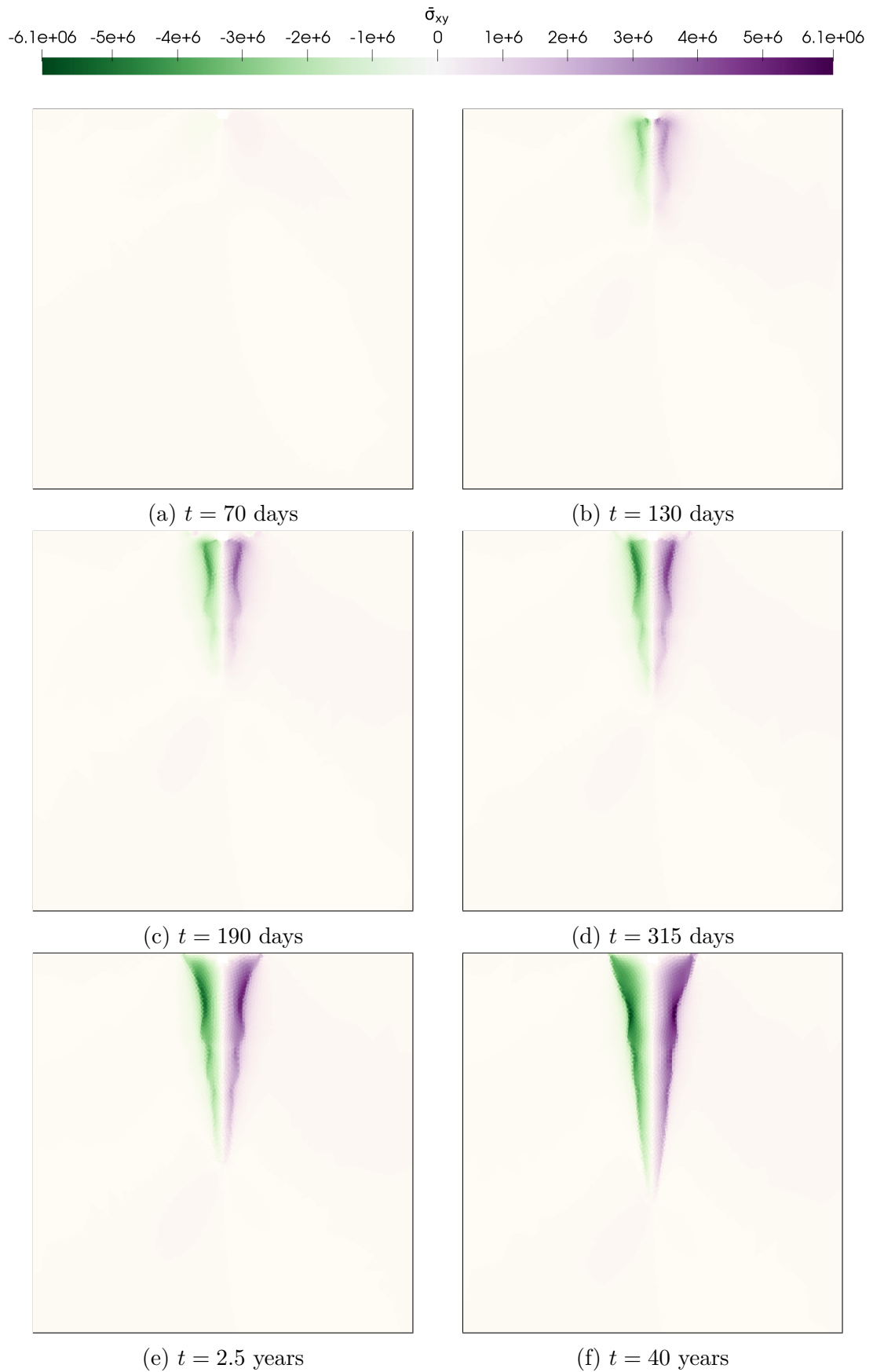


Figure 2.21: The evolution of the  $\bar{\sigma}_{xy}$  component of the effective Cauchy stress tensor, of the water-free crevasse propagation with default parameter values and increased longitudinal stress.

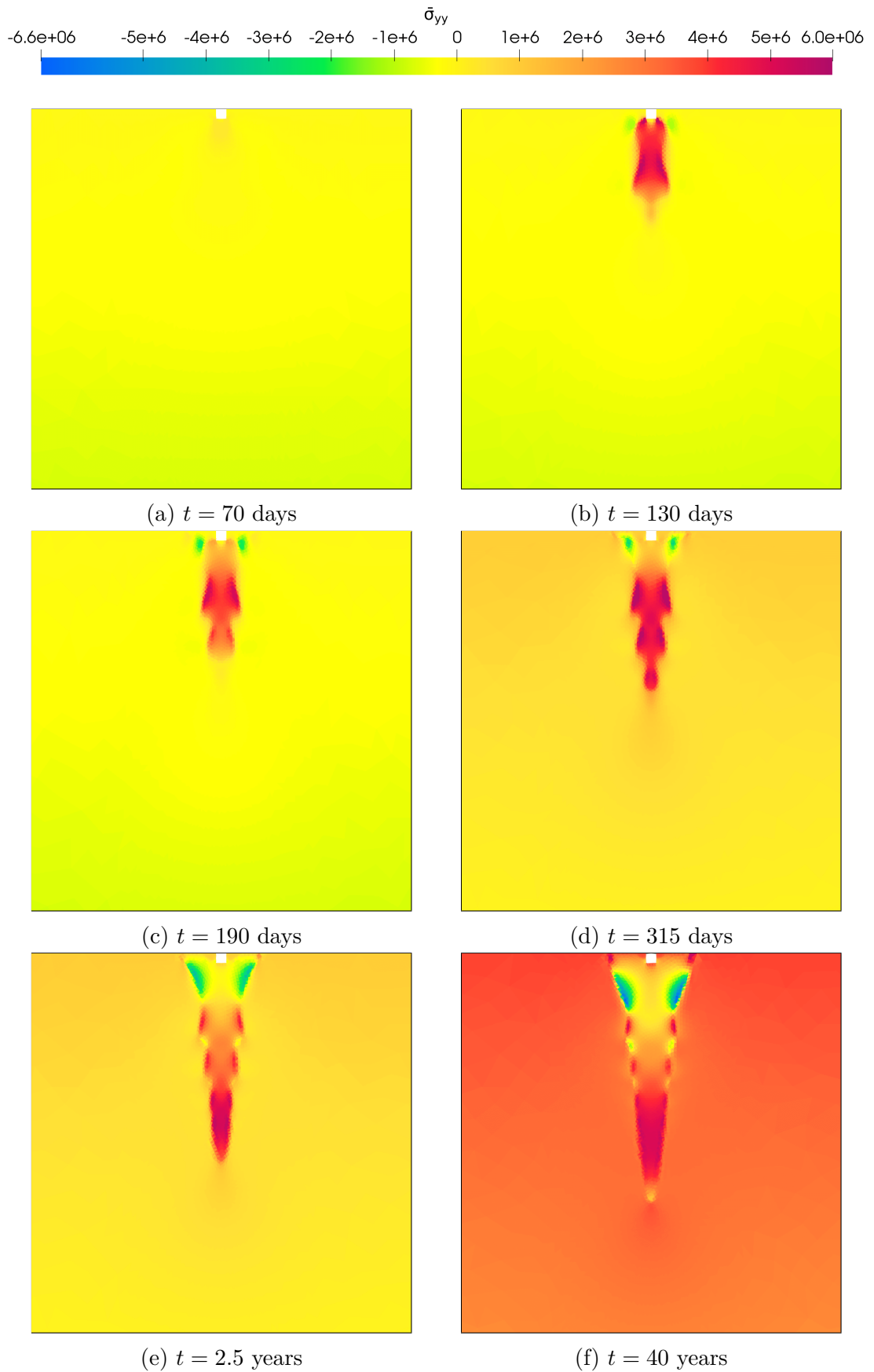


Figure 2.22: The evolution of the  $\bar{\sigma}_{yy}$  component of the effective Cauchy stress tensor, of the water-free crevasse propagation with default parameter values and increased longitudinal stress.

## 2.4 Water-free vs. Water-filled Crevasse

Let us now demonstrate the hydrofracturing effect. So far we assumed cracks to be water-free, which corresponds to setting  $p_w = 0$  in equation 1.8 (resp. 1.2). Now, we are going to compare the reference simulation with the case, when  $p_w$  is set to  $p_w(d) = \rho_w g d$ , which corresponds to a crack that is completely filled with water throughout its whole evolution.

Fig. 2.23 shows the comparison of  $D$  in several time snapshots for two cases - water-free (left column) and water-filled (right column), both with model parameters at their default values (tab. 2.1), with  $D$  presented in a logarithmic scale. As one can see, the water-filled crevasse penetrated through the whole ice slab in almost 11 years, in contrast to water-free crack. The quantitative analysis of the crack penetration is better represented by figure 2.24, which shows the crevasse depth as a function of time for both mentioned cases -  $D^w$  represents the respective levels of the lowermost point of selected damage iso-contour for water-filled case, while  $D$  marks the standard water-free setup. It can be seen that the water-filled crevasse propagates relatively slowly in approximately the first 10.5 years of the simulation and then spread rapidly in a range of months until it reaches the bottom of the ice slab. Penetrating through the whole domain in the water-filled case matches with the conclusion of Weertman (1973) that "... there is no limit to the depth of an isolated water-filled crevasse. There is no reason why such a crevasse may not penetrate the bottom surface of a glacier."

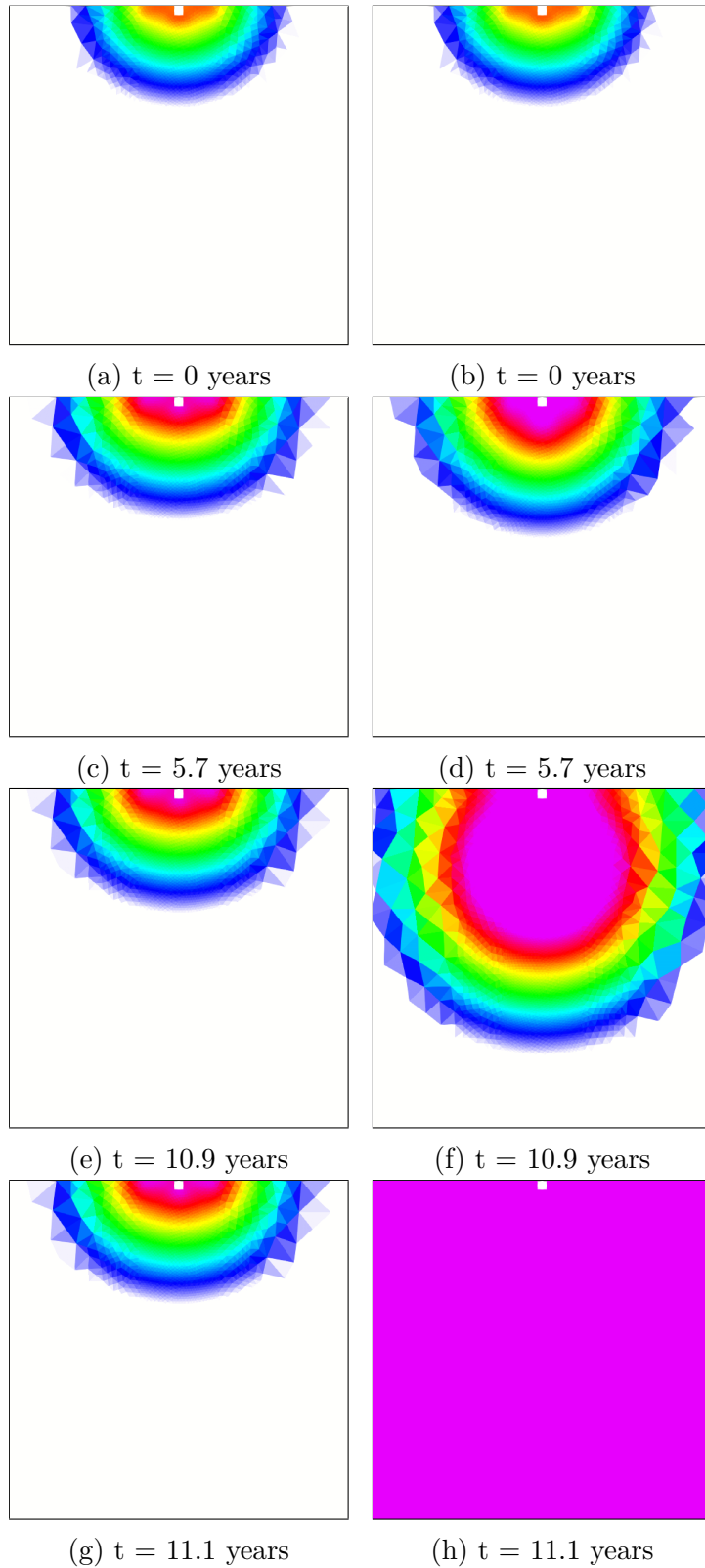
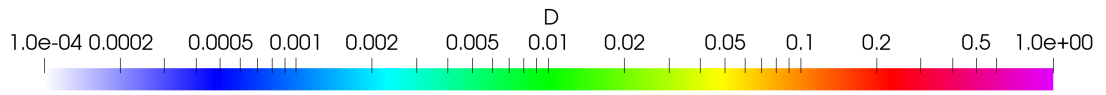


Figure 2.23: The evolution of a water-free (left column) vs. water-filled (right column) crevasse.

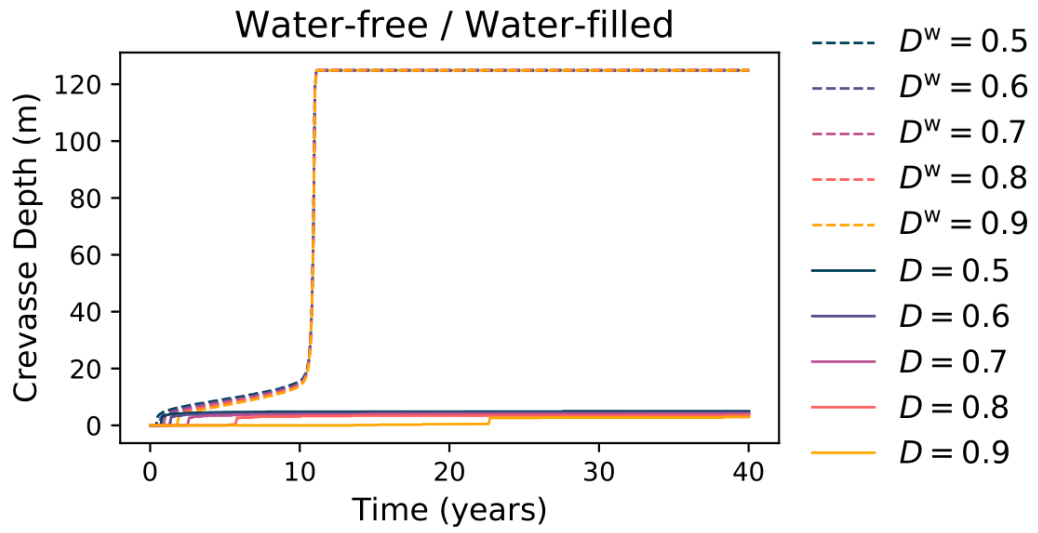


Figure 2.24: The crevasse depth evolution of a water-filled vs. water-free crevasse.

# Conclusion

This thesis deals with the continuum poro-damage mechanics (CPDM) and its application in the investigation of ice crack propagation using the finite element method (FEM). The essential principle of the CPDM is the description of the crack via a single scalar field (the damage  $D$ ) Duddu et al. (2020). In this study, we considered the linear elastic rheology of the ice and did not concern the temperature effects.

After formulating the governing equations of the problem (subsection 1.2.2) and of the corresponding weak formulation (subsection 1.3.2), we present the model setup - domain geometry and boundary and initial conditions. The boundaries are subject to two free-slip and two Neumann boundary conditions, while the initial state reflects a small top surface crack (see fig. 1.1). The numerical implementation consists of using the FEM-based open-source library package - FEniCS (Alnaes et al., 2015).

The first studied feature of the model was its sensitivity to model parameters:  $dt$  (time step size),  $l_c$  (length scale parameter), a mesh resolution, the WDAZ (the width of damage active zone), and the IDA (the initially damaged area). The most notable effect on the water-free crevasse propagation was observed for parameters  $l_c$  and the WDAZ, with the IDA parameter having a substantial effect only for shallow crevasses.

The second investigated process is the dependence of the water-free crevasse depth propagation on the aforementioned model parameters. The conclusion is that parameters  $l_c$  and the IDA have the most significant effect on the crevasse's final depth, with  $dt$  and the WDAZ having a small effect and the mesh resolution having almost none.

The application of the additional longitudinal tensile stress  $\sigma_+$  (regarding a top water-free crevasse) allowed us to discuss and compare the numerical results for the maximal depth of top water-free crevasse with the linear elastic fracture mechanics predictions (Weertman, 1973). While the relative error is significant considering the shallow crevasse case (up to 62 %), the numerical results for the deep crevasse are following the LEFM with relative error reaching max. 5.1 %. For  $\sigma_+$  application, we also provide the evolution of other model related physical quantities (subsection 2.3.2).

The simulation of the water-filled crevasse confirms the conclusion formulated by Weertman (1973) that a single top-based water-filled crevasse can reach the bottom of a freely floating ice slab.

The preparation and usage of the model for future planetary applications should follow further model testing and calibration, its reformulation for basal water-filled crevasse, and another testing for basal crevasses. Note that introducing a viscosity into the model may be necessary. After calibration of the basal crevasse cases, the final version of the model shall be applied on icy moons conditions to investigate the possibility of the hydrofracturing of the outer shells of icy moons, particularly Europa and Enceladus in response to mechanical loading by tidal, or as a result of pressurizing the internal ocean.

# Bibliography

- A. A. Hillerborg, M. Mod er, and P.-E. Petersson. Analysis of crack formation and crack growth in concrete by means of fracture mechanics and finite elements. *Cement and Concrete Research*, 6(6):773–781, 1976.
- J. Ahrens, B. Geveci, and Ch. Law. *ParaView: An End-User Tool for Large-Data Visualization*. Elsevier-Butterworth-Heinemann, Burlington, 2005. ISBN 9780123875822.
- M. S. Alnaes, J. Blechta, J. Hake, A. Johansson, B. Kehlet, A. Logg, C. Richardson, J. Ring, M.E. Rognes, and G. N. Wells. The fenics project version 1.5. *Archive of Numerical Software*, 3, 2015.
- K. J. Bathe. *Finite Element Procedures*. Prentice Hall, 2006. ISBN 9780979004902.
- M. Beuthe. Enceladus’s crust as a non-uniform thin shell: I tidal deformations. *Icarus*, 302:145–174, 2018.
- G. D. Crawford and D. J. Stevenson. Gas-driven water volcanism and the resurfacing of europa. *Icarus*, 73(1):66–79, 1988.
- R. Duddu and H. Waisman. A temperature dependent creep damage model for polycrystalline ice. *Mechanics of Materials*, 46:23–41, 2012.
- R. Duddu and H. Waisman. A nonlocal continuum damage mechanics approach to simulation of creep fracture in ice sheets. *Computational Mechanics*, 51(6): 961–974, 2013.
- R. Duddu, S. Jim nez, and J. Bassis. A non-local continuum poro-damage mechanics model for hydrofracturing of surface crevasses in grounded glaciers. *Journal of Glaciology*, 66(257):415–429, 2020.
- D. R. Hayhurst. Creep rupture under multi-axial states of stress. *Journal of the Mechanics and Physics of Solids*, 20(6):381–382, 1972.
- R. Hock. Glacier melt: a review of processes and their modelling. *Progress in Physical Geography: Earth and Environment*, 29(3):362–391, 2005.
- S. Jim nez, R. Duddu, and J. Bassis. An updated-Lagrangian damage mechanics formulation for modeling the creeping flow and fracture of ice sheets. *Computer Methods in Applied Mechanics and Engineering*, 313:406–432, 2017.
- L. Kachanov. *Time of the Rupture Process under Creep Conditions*. Izvestiia Akademii Nauk SSSR, Otdelenie Teckhnicheskikh Nauk, 1958.
- K. Kalousova, O. Sou ek, G. Tobie, G. Choblet, and O.  adek. Water generation and transport below europa’s strike-slip faults. *Journal of Geophysical Research: Planets*, 121(12):2444–2462, 2016.

- M. J. Krawczynski, M. D. Behn, S. B. Das, and I. Joughin. Constraints on the lake volume required for hydro-fracture through ice sheets. *Geophysical Research Letters*, 36, 2009.
- J. Krug, J. Weiss, O. Gagliardini, and G. Durand. Combining damage and fracture mechanics to model calving. *The Cryosphere*, 8(6):2101–2117, 2014.
- S. Lee, R. T. Pappalardo, and N. C. Makris. Mechanics of tidally driven fractures in europa’s ice shell. *Icarus*, 177(2):367–379, 2005. Europa Icy Shell.
- Z. Martinec. *Principles of Continuum Mechanics*. Nečas Center Series. Birkhäuser, Cham, 2019. ISBN 9783030053901.
- M. E. Mobasher, R. Duddu, J. N. Bassis, and H. Waisman. Modeling hydraulic fracture of glaciers using continuum damage mechanics. *Journal of Glaciology*, 62(234):794–804, 2016.
- S. Murakami, M. Kawai, and H. Rong. Finite element analysis of creep crack growth by a local approach. *International Journal of Mechanical Sciences*, 30(7):491–502, 1988.
- G. W. Ojakangas and D. J. Stevenson. Thermal state of an ice shell on europa. *Icarus*, 81(2):220–241, 1989.
- W. Paterson. *The Physics of Glaciers*. 3rd Edition. Pergamon-Elsevier, Oxford, 1994. ISBN 9781483287256.
- A. Pralong and M. Funk. Dynamic damage model of crevasse opening and application to glacier calving. *Journal of Geophysical Research: Solid Earth*, 110(B1), 2005.
- Y. N. Rabotnov. Paper 68: On the equation of state of creep. *Proceedings of the Institution of Mechanical Engineers, Conference Proceedings*, 178(1):2117–2122, 1963.
- M. L. Rudolph and M. Manga. Fracture penetration in planetary ice shells. *Icarus*, 199(2):536–541, 2009.
- R. A. Smith. The application of fracture mechanics to the problem of crevasse penetration. *Journal of Glaciology*, 17(76):223–228, 1976.
- C. J. van der Veen. Fracture mechanics approach to penetration of bottom crevasses on glaciers. *Cold Regions Science and Technology*, 27(3):213–223, 1998a.
- C. J. van der Veen. Fracture mechanics approach to penetration of surface crevasses on glaciers. *Cold Regions Science and Technology*, 27(1):31–47, 1998b.
- J. Weertman. Deformation of floating ice shelves. *Journal of Glaciology*, 3:38–42, 1957.
- J. Weertman. Can a water-filled crevasse reach the bottom surface of a glacier. *International Association of Scientific Hydrology*, 95:139–145, 1973.

- J. Weiss. Scaling of fracture and faulting of ice on earth. *Surveys in Geophysics*, 24(2):185–227, 2003.
- J. Weiss. Subcritical crack propagation as a mechanism of crevasse formation and iceberg calving. *Journal of Glaciology*, 50:109–115, 2004.

# List of Figures

1	Europa and Enceladus. (Credit: NASA.) . . . . .	3
2	Hydrofracturing. (Credit: NASA.) . . . . .	3
1.1	The illustration of a studied model geometry. . . . .	9
2.1	The effect of time step $dt$ size on crevasse propagation. . . . .	18
2.2	The effect of $l_c$ parameter on crevasse propagation. . . . .	18
2.3	The effect of a mesh resolution on crevasse propagation. . . . .	18
2.4	The effect of the WDAZ on crevasse propagation. . . . .	19
2.5	The effect of the IDA on crevasse propagation. . . . .	19
2.6	The comparison of the evolution of the depth of water-free crevasse with respect to the time step $dt$ size. . . . .	22
2.7	The comparison of the evolution of the depth of water-free crevasse with respect to the length scale parameter $l_c$ . . . . .	23
2.8	The comparison of the evolution of the depth of water-free crevasse with respect to the mesh resolution. . . . .	24
2.9	The comparison of the evolution of the depth of water-free crevasse with respect to the WDAZ. . . . .	25
2.10	The comparison of the evolution of the depth of water-free crevasse with respect to the size of the IDA. . . . .	26
2.11	The crevasse evolution of two different tensile stress cases - $\sigma_{xx}$ and $\sigma_{xx} + \sigma_+$ . . . . .	28
2.12	The crevasse depth evolution of two different tensile stress cases - $\sigma_{xx}$ and $\sigma_{xx} + \sigma_+$ . . . . .	29
2.13	The evolution of the damage $D$ quantity. . . . .	31
2.14	The evolution of the damage rate $\dot{D}$ . . . . .	32
2.15	The evolution of the local damage increment $\dot{D}^{loc} \cdot dt$ . . . . .	33
2.16	The evolution of the effective maximum principal stress $\bar{\sigma}^{(I)}$ . . . . .	34
2.17	The evolution of the effective von Mises stress $\bar{\sigma}^v$ . . . . .	35
2.18	The evolution of the effective Hayhurst stress $\bar{\chi}$ . . . . .	36
2.19	The evolution of the effective pressure $\bar{p}$ . . . . .	37
2.20	The evolution of the $\bar{\sigma}_{xx}$ component of the effective Cauchy stress tensor. . . . .	38
2.21	The evolution of the $\bar{\sigma}_{xy}$ component of the effective Cauchy stress tensor. . . . .	39
2.22	The evolution of the $\bar{\sigma}_{yy}$ component of the effective Cauchy stress tensor. . . . .	40
2.23	The evolution of a water-free vs. water-filled crevasse. . . . .	42
2.24	The crevasse depth evolution of a water-filled vs. water-free crevasse. . . . .	43

# List of Tables

1.1	The overview of physical parameters used for simulation of the damage propagation. . . . .	11
2.1	The overview of model parameters used for simulation of the damage propagation. . . . .	16
2.2	The depth comparison of the theoretical prediction with the FEM results for top water-free crevasses. . . . .	29

# List of Abbreviations

BC	boundary condition
CDM	continuum damage mechanics
CPDM	continuum poro-damage mechanics
FEM	finite element method
IC	initial condition
IDA	initially damage area
LEFM	linear elastic fracture mechanics
PDEs	partial differential equations
RVE	representative volume element
WDAZ	width of damage active zone

# A. Attachments

## A.1 The LEFM Approach

The traditional approach to describe ice crevasses is the linear elastic fracture mechanics (LEFM). The existence of bottom crevasses was suggested for the first time in 1973 by Weertman (1973). The principle comes from the idea that bottom crevasses on floating glaciers are filled with seawater. Consequently, the water pressure in the crevasse partially balances the weight-induced lithostatic stress, which otherwise prevents crevasse propagation.

According to Weertman (1973), an isolated water-free crevasse on the top of a semi-infinite ice slab subject to gravity can penetrate to maximal depth  $L_{max}^{top}$  given by

$$L_{max}^{top} = \frac{\pi}{2 \rho_i g} \sigma_{xx}, \quad (\text{A.1})$$

where  $\sigma_{xx}$  is the far-field tensile stress. Building up on the  $L_{max}^{top}$  given by equation A.1, we can apply the tensile stress  $\sigma_{xx}$  from van der Veen (1998a), where he uses the tensile stress of free-floating ice as

$$\sigma_{xx} = \frac{1}{2} \rho_i g H - \frac{1}{2} \frac{\rho_i^2}{\rho_w} g H. \quad (\text{A.2})$$

This expression represents an estimate of the dynamic tensional stress for a freely-floating ice slab. By substituting equation A.2 into A.1, we get the maximal length of a single water-free crevasse in a floating ice shelf, which can be useful for calibration of continuum (poro-) damage mechanics (CDM or CPDM, respectively) based models

$$L_{max}^{top} = \frac{\pi H}{4} \frac{\rho_w - \rho_i}{\rho_w}. \quad (\text{A.3})$$